REPORT DOCUMENTATION PAGE

1. REPORT DATE (DD-MM-YYYY)	2. REPORT TYPE	3. DATES COVERED (From - To)
6/15/2007	Final Report	3/1/04-4/30/07

4. TITLE AND SUBTITLE	5a. CONTRACT NUMBER
An Oriented-Eddy Collision Model for Turbulence Prediction	
	5b. GRANT NUMBER
	N00014-04-1-0267
	5c. PROGRAM ELEMENT NUMBER

6. AUTHOR(S)	5d. PROJECT NUMBER
Blair Perot	
	5e. TASK NUMBER
	5f. WORK UNIT NUMBER

7. PERFORMING ORGANIZATION NAME(S) AND ADDRESS(ES)	8. PERFORMING ORGANIZATION REPORT NUMBER
University of Massachusetts, Amherst	

9. SPONSORING/MONITORING AGENCY NAME(S) AND ADDRESS(ES)	10. SPONSOR/MONITOR'S ACRONYM(S)
ONR, Ron Joslin, Ballston Centre Tower One 800 North Quincy Street Arlington VA 22217-5660	
	11. SPONSOR/MONITOR'S REPORT NUMBER(S)

12. DISTRIBUTION/AVAILABILITY STATEMENT

DISTRIBUTION STATEMENT A
Approved for Public Release
Distribution Unlimited

13. SUPPLEMENTARY NOTES

14. ABSTRACT

Describes a the development of an entirely new approach to modeling turbulence, that has far less empiricism and contains more physics, but costs far less than large eddy simulation.

15. SUBJECT TERMS

Turbulence modeling.

16. SECURITY CLASSIFICATION OF:			17. LIMITATION OF ABSTRACT	18. NUMBER OF PAGES	19a. NAME OF RESPONSIBLE PERSON
a. REPORT	b. ABSTRACT	c. THIS PAGE			
					19b. TELEPHONE NUMBER (Include area code)

INSTRUCTIONS FOR COMPLETING SF 298

1. REPORT DATE. Full publication date, including day, month, if available. Must cite at least the year and be Year 2000 compliant, e.g. 30-06-1998; xx-06-1998; xx-xx-1998.

2. REPORT TYPE. State the type of report, such as final, technical, interim, memorandum, master's thesis, progress, quarterly, research, special, group study, etc.

3. DATES COVERED. Indicate the time during which the work was performed and the report was written, e.g., Jun 1997 - Jun 1998; 1-10 Jun 1996; May - Nov 1998; Nov 1998.

4. TITLE. Enter title and subtitle with volume number and part number, if applicable. On classified documents, enter the title classification in parentheses.

5a. CONTRACT NUMBER. Enter all contract numbers as they appear in the report, e.g. F33615-86-C-5169.

5b. GRANT NUMBER. Enter all grant numbers as they appear in the report, e.g. AFOSR-82-1234.

5c. PROGRAM ELEMENT NUMBER. Enter all program element numbers as they appear in the report, e.g. 61101A.

5d. PROJECT NUMBER. Enter all project numbers as they appear in the report, e.g. 1F665702D1257; ILIR.

5e. TASK NUMBER. Enter all task numbers as they appear in the report, e.g. 05; RF0330201; T4112.

5f. WORK UNIT NUMBER. Enter all work unit numbers as they appear in the report, e.g. 001; AFAPL30480105.

6. AUTHOR(S). Enter name(s) of person(s) responsible for writing the report, performing the research, or credited with the content of the report. The form of entry is the last name, first name, middle initial, and additional qualifiers separated by commas, e.g. Smith, Richard, J, Jr.

7. PERFORMING ORGANIZATION NAME(S) AND ADDRESS(ES). Self-explanatory.

8. PERFORMING ORGANIZATION REPORT NUMBER. Enter all unique alphanumeric report numbers assigned by the performing organization, e.g. BRL-1234; AFWL-TR-85-4017-Vol-21-PT-2.

9. SPONSORING/MONITORING AGENCY NAME(S) AND ADDRESS(ES). Enter the name and address of the organization(s) financially responsible for and monitoring the work.

10. SPONSOR/MONITOR'S ACRONYM(S). Enter, if available, e.g. BRL, ARDEC, NADC.

11. SPONSOR/MONITOR'S REPORT NUMBER(S). Enter report number as assigned by the sponsoring/ monitoring agency, if available, e.g. BRL-TR-829; -215.

12. DISTRIBUTION/AVAILABILITY STATEMENT. Use agency-mandated availability statements to indicate the public availability or distribution limitations of the report. If additional limitations/ restrictions or special markings are indicated, follow agency authorization procedures, e.g. RD/FRD, PROPIN, ITAR, etc. Include copyright information.

13. SUPPLEMENTARY NOTES. Enter information not included elsewhere such as: prepared in cooperation with; translation of; report supersedes; old edition number, etc.

14. ABSTRACT. A brief (approximately 200 words) factual summary of the most significant information.

15. SUBJECT TERMS. Key words or phrases identifying major concepts in the report.

16. SECURITY CLASSIFICATION. Enter security classification in accordance with security classification regulations, e.g. U, C, S, etc. If this form contains classified information, stamp classification level on the top and bottom of this page.

17. LIMITATION OF ABSTRACT. This block must be completed to assign a distribution limitation to the abstract. Enter UU (Unclassified Unlimited) or SAR (Same as Report). An entry in this block is necessary if the abstract is to be limited.

Final Report: An Oriented-Eddy Collision Model for Turbulence Prediction

Graduate Students: RaeAnn Andeme, Venkat Subramanian,

Summary

The exact governing equations of fluid dynamics are too computationally expensive to solve on a computer for practical applications. They will remain intractable for at least the next 50 years. In order to computationally predict the performance of engineering applications that involve fluids, alternative (and computationally tractable) equations must be formulated. These equations are referred to as turbulence models.

This project has successfully developed an entirely new theory and computational approach to modeling turbulence. The idea was to track a statistical ensemble of colliding and spinning disks (oriented eddies) in colloidal suspension in the fluid. This somewhat usual fluid model (akin to the flow of liquid crystals) was chosen because we observed the remarkable property that this type of non-Newtonian fluid behaves just like a turbulent fluid in the rapid distortion (large mean flow gradients) limit.

The project was successful in demonstrating that with appropriate extensions this model of turbulence could be applied to a very wide variety of turbulent flows with high predictive accuracy. A number of different limits in which the model is exact were demonstrated. We were also successful in keeping the number of model constants very low. In addition, the theory behind the model was vastly expanded when we were able to show that this approach is equivalent to a model for the evolution of the two-point velocity correlation tensor.

The prediction (or modeling) of turbulent fluid flow is arguably one of the greatest bottlenecks in the Navy's ability to rapidly design innovative devices and respond to environmental threats[73]. While this research does not address a specific Navy operational issue, it has an extremely broad reaching impact on Navy operations in general and will enhance the Navy's ability to successfully execute its mission.

Background

One of the greatest bottlenecks in Engineering Design today is the computational prediction of turbulent fluids. In a vast variety of applications: from air pollution, to engine efficiency and emissions, to global climate prediction, to submarine performance, to galactic evolution, turbulence plays a critical, if not the most important, physical role. Some of these problems will never be computationally tractable without a turbulence model. Those that do become tractable in the coming decades (using perhaps large eddy simulation) will then represent a stunning waste of resources that could be used more productively for testing and optimizing multiple designs or adding additional physics.

In theory, low cost turbulence models that are predictive could have a profound effect on how computational fluid dynamics (CDF) is used in the design process. CFD could go from being a qualitative predictor of trends to a pervasive qualitative design tool comparable to Finite Elements and computational mechanics. While existing engineering turbulence models do not currently provide predictive accuracy, it is demonstrated in this proposal that by modeling the turbulence structure as well as the fluctuating velocity magnitudes the Oriented-Eddy Collision (OEC) model is able predict the influence of the mean flow on the turbulence exactly. Since this is the dominant physical effect on the turbulence evolution, the OEC model is highly predictive (only turbulence-turbulence interactions require modeling and this process is relatively well understood). The price for this predictive accuracy is an order of magnitude increase in the cost of the model compared to traditional approaches. This puts the model cost at a few times the cost of the mean flow calculation (which is appropriate given the critical physics contained within the turbulence) and many orders of magnitude less expensive than large eddy simulation (LES) or direct numerical simulation (DNS) solutions. This is a region of the cost/performance parameter space that has not been extensively explored previously in the context of turbulence modeling and which holds great promise.

Significance & Objectives

The computational resources required to solve the governing equations of fluid dynamics, the Navier-Stokes equations, increase as the cube of the Reynolds number (Rogallo & Moin). If large eddy simulation (LES) models are eventually successful this exponent could be reduced. Still, LES of a passenger jet wing is not expected to be possible on the largest supercomputer until around 2045 (Spalart). This assumes current increases in computer speed, which may well not continue. Most environmental problems have much larger Reynolds numbers and may never be computationally tractable with these approaches. Even problems that do become tractable are a waste of resources in the context of Engineering Design where Computational Fluid Dynamics (CFD) has the potential to be the most useful. Computing a few engineering parameters (such as wing drag) with LES and the supercomputer of the year 2045 is akin to swatting a fly with a nuclear bomb. These resources could be used much more effectively to optimize the design or add additional physics. Computers are having a profound effect on engineering design, but progress on problems involving fluids has been, and will remain, stalled indefinitely until cost-effective and predictive turbulence models are developed.

The purpose of this project was to develop a turbulence model that included more physics (thereby increasing the predictive accuracy) while at the same time drastically reducing the number of empirically determined model constants. This comes at a significant computational price, but not a price that is out of line with the importance of the turbulent physics that the model is required to represent. It is a price which is many orders of magnitude less than LES or DNS, and yet still provides the predictive accuracy necessary to move CFD from being a qualitative predictor of trends, to a pervasive quantitative design tool comparable in utility to current day Finite Elements in computational mechanics.

Classical Turbulence Modeling

The coarse-grained equations for incompressible fluid flow are given by,

$$\bar{u}_{i,t} + (\overline{u_i u_j})_{,j} = -\bar{p}_{,i} + v\bar{u}_{i,jj} - (\overline{u_i u_j} - \bar{u}_i \bar{u}_j)_{,j} \tag{1a}$$

$$\bar{u}_{i,i} \tag{1b}$$

These look almost the same as the original governing Navier-Stokes equations except for the final source term in the momentum equation. The tensor in the final term represents the influence of the unresolved turbulent fluctuations on the coarse-grained velocity evolution. When a Reynolds (ensemble) average is used $R_{ij} = \overline{u_i u_j} - \bar{u}_i \bar{u}_j$ is referred to as the Reynolds stress tensor. In large eddy simulation, this quantity is referred to as the subgrid-scale stress tensor.

The Reynolds stress tensor is the critical unknown that results from coarse-graining the Navier-Stokes equations. It describes how turbulent fluctuations influence the mean (or resolved/coarse) flow evolution. Once a model for the Reynolds stress tensor is formulated these equations are much easier to solve computationally than the original Navier-Stokes equations. Most importantly, when mesh adaptation is employed the computational cost does not scale with Reynolds number. These equations look like the Reynolds Averaged Navier-Stokes (RANS) equations formulated over a century ago (Reynolds). However, it has recently been recognized that these equations hold for any type of coarse graining (not just the Reynolds ensemble average), and are directly applicable to LES (Germano). Since the fundamental modeling problem and equations are the same for both RANS and LES, the model discussed in this proposal is equally applicable (and actually very well suited except for its cost) to LES.

In the context of turbulence modeling the workhorse of both commercial and in-house Computational Fluid Dynamics (CFD) codes is the two-equation models, most notably the K-ε model. These models involve modeled partial differential transport equations for two scalar turbulence quantities (most often the turbulent kinetic energy, K, and dissipation rate, ε). There is also a hypothesized algebraic constitutive equation relating these two scalar quantities and the mean (or coarse) flow information to the Reynolds stress tensor. In many respects, the predictive performance of two-equation models is phenomenally impressive given the complexity of the physical process that they are charged with representing. They work quite well predicting basic turbulence producing regions such as simple boundary layers and free shear layers. The modifications based

3

on renormalization group theory (Orzag & Yakhot) and elliptic relaxation (Durbin) have even expanded the predictive scope of these models. Nevertheless, it is well understood at this time, even by CFD users, that the physics contained in these models is fundamentally limited. These types of models are incapable of predicting with real predictive accuracy the wide variety of turbulent conditions found in real engineering design applications.

It was expected that Reynolds Stress Transport (RST) models would perform considerably better. These models do not use a hypothesized constitutive equation for the Reynolds stress tensor. Instead, they start with the exact (but unclosed) transport equation for the Reynolds (or subgrid scale) stress tensor,

$$R_{ij,t} + \bar{u}_k R_{ij,k} = \nu R_{ij,kk} - (R_{jk}\bar{u}_{i,k} + R_{ik}\bar{u}_{j,k})$$
$$-\overline{u'_i u'_j u'_k}_{,k} - \overline{(p'_{,i}u'_j + p'_{,j}u'_i)} - 2\nu\overline{u'_{i,k},u'_{j,k}} \tag{2}$$

The last three source terms (the transport term, the pressure term, and the dissipation term) require modeling. The lack of an *ad hoc* constitutive equation is a very important step, but just as important is the fact that the influence of the mean flow on the turbulence evolution (the second term on the right hand side of the transport equation) is closed and does not require a model. Mean flow gradients are the primary mechanism for turbulence generation and this equation suggests that this mechanism is exactly captured.

Unfortunately, the predictive promise of RST models has not been realized and while RST models are available in most CFD codes they are rarely used. In practice, their predictive performance is rarely better than the more computationally robust two-equation models. The problem lies in the fact that the pressure term also carries information about the mean flow gradients which is just as important as the explicit production term but which is extremely difficult to model. The effect of the mean flow gradients is therefore **not** exactly captured. The modeled pressure term must capture those effects. It has even been shown that modeling this term is fundamentally impossible in certain circumstances using only the information provided by the RST models (Reynolds, Speziale). In addition to this fundamental shortcoming RST models have another significant source of error and uncertainly. This is the *ad hoc* transport equation (usually an ε equation) that is required to close the system. Other issues exist but these two effects (the pressure-term and additional transport equation) represent the majority of empirical model constants and predictive uncertainty in RST models.

The Problem with Classical Models

Some typical results for a RST model are shown in Figure 1. In each of these situations, homogeneous isotropic turbulence is subjected to a very simple arrangement of mean flow gradients. Depending on the particular arrangement of mean flow strains, certain components of the Reynolds stress tensor are amplified with time and others decrease. In Figure 1, the circles are direct numerical simulation (DNS) data and the lines are the corresponding RST model predictions. In some cases, the model predictions are quite accurate; however, in others the agreement is poor. The level of predictive performance can be characterized by the dimensionless velocity gradient, $S^* = (\bar{u}_{i,j}\bar{u}_{i,j})^{1/2} K / \varepsilon$. This
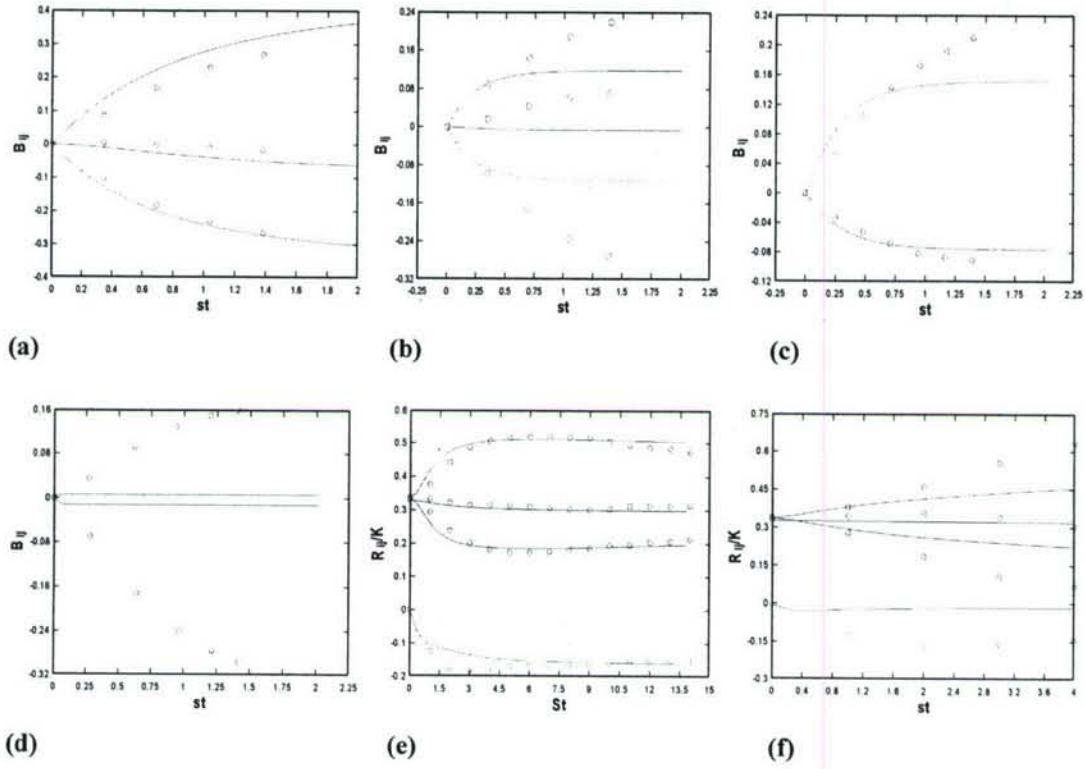
Figure 1: State-of-the-art RST model predictions of turbulence subjected to simple mean flows. Dimensionless normalized shear stress as a function of dimensionless time. Symbols are experimental or DNS data and lines are RST model predictions. (a) plain strain, $S^* = 0.5$ (b) plain strain, $S^* = 4$ (c) axisymmetric contraction, $S^* = 4.08$ (d) axisymmetric expansion, $S^* = 55.8$ (f) homogeneous shear, $S^* = 4.71$, (f) homogeneous shear, $S^* = 30.9$. Data of cases (a-d) are from Lee & Reynolds and (e-f) from Matsumoto.

is a ratio of the turbulence response time to the mean flow time scale. If S^* is small the turbulence response time is much less than the time over which the mean flow changes appreciably. In this case, the turbulence is always in quasi-equilibrium with the mean flow (since it can respond much more quickly than the mean flow is changing) and the RST model performs well. However, when the turbulence is subjected to rapid changes the model performs poorly. RST models are fundamentally quasi-equilibrium models.

There are many flow situations such as turbulent boundary layers and shear layers where the flow is in quasi-equilibrium. However, in engineering applications there are usually critical flow regions where quasi-equilibrium is not a good approximation. These include separating flows, transition, reattaching flows, fast moving boundaries (such as turbine blades) and flows under the influence of strong body forces such as gravity or electromagnetic forces. While the non-equilibrium regimes occupy less volume in a typical CFD calculation that the quasi-equilibrium regimes they often dominate the critical physics and frequently dictate the overall predictive performance of the turbulence model. Figure 2a shows a pictorial representation of parameter space.
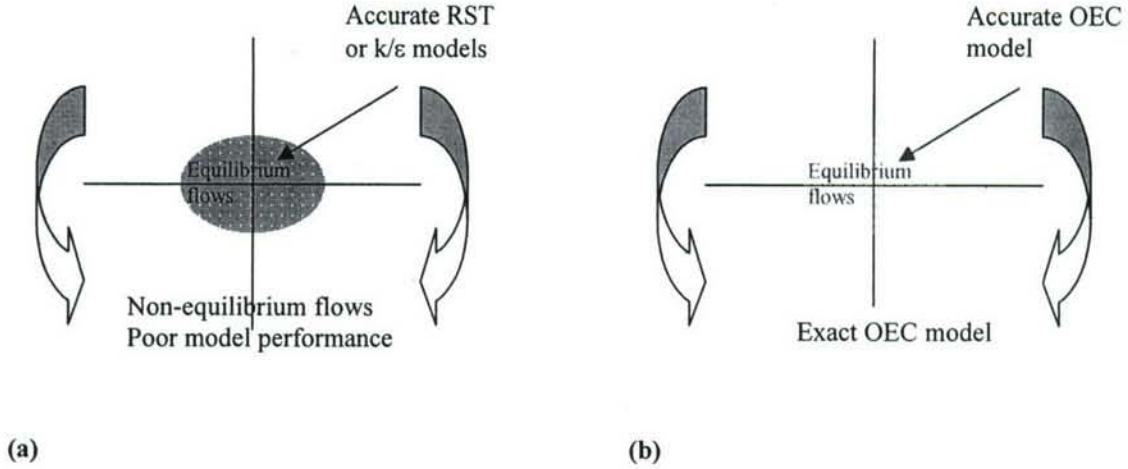
Figure 2: Pictorial representation of state-space and the regions of applicability of (a) traditional engineering turbulence models and (b) the eddy interaction model. Traditional models perform well close to the origin where the turbulence is in quasi-equilibrium with the mean flow and/or external forces. The OEC model increases the range of predictive performance significantly by exactly capturing mean flow (or external force) effects that dominate when the flow is not in equilibrium.

Traditional turbulence models are predictive only near the origin of this diagram where the flow is close to some equilibrium state.

What is most interesting is that the highly non-equilibrium regime should be the easier regime to model. A high degree of nonlinearity implies a strong separation of time scales, which in turn implies that course graining could be accomplished very accurately. While turbulence does not contain a separation of length scales (the large turbulent length scales are always the same order of magnitude as the mean flow length scales), it sometimes does contain this time scale separation that can be advantageous. The OEC model described below is exact in the limit of very strong mean flow gradients (the non-equilibrium limit). As shown in Figure 2b, this implies that very far from the origin of the diagram the model is exact. This type of model is inherently much more predictive.

The influence of the mean flow on the turbulence (or Reynolds stress tensor) evolution is a linear process (only turbulence-turbulence interactions are nonlinear). Therefore, in theory, it should be possible to capture this effect exactly, and this is indeed the case. The key insight that is necessary to do this is to recognize that although the Reynolds stress tensor contains sufficient information to describe the turbulence effects on the mean flow it does not contain enough information to correctly represent the influence of the mean flow on the turbulence[11]. To capture the influence of the mean flow exactly the model must also capture the effect of the mean flow gradients on the turbulence structure.

The Solution

In this work, we use two-point correlations as a measure of turbulence structure. If two nearby points in a physical domain have a very high correlation between their velocities,

6

this implies that turbulence structures tend to be aligned with the line joining those two points. If two points have a low or negative velocity correlation, it implies that the turbulence structure does not span the distance between those two points.

One major result of this project has been the discovery that the OEC model is related to the exact two-point correlation equation.

$$C_{ij,t}(\mathbf{x},\mathbf{r}) = -\overline{u}_{i,k}(\mathbf{x})C_{kj} - \overline{u}_{j,k}(\tilde{\mathbf{x}})C_{ik} - \overline{u}_k(\mathbf{x})\frac{\partial C_{ij}}{\partial x_k} + \left(\overline{u}_k(\mathbf{x}) - \overline{u}_k(\tilde{\mathbf{x}})\right)\frac{\partial C_{ij}}{\partial r_k}$$
$$-\left(\frac{\partial T_{(ik)j}}{\partial x_k} - \frac{\partial T_{(ik)j}}{\partial r_k}\right) - \frac{\partial T_{i(jk)}}{\partial r_k} - \left(\frac{\partial \overline{pu_j'}}{\partial x_i} - \frac{\partial \overline{pu_j'}}{\partial r_i}\right) - \frac{\partial \overline{u_i'p}}{\partial r_j} + \nu\left(\frac{\partial^2 C_{ij}}{\partial x_k \partial x_k} - 2\frac{\partial^2 C_{ij}}{\partial x_k \partial r_k} + 2\frac{\partial^2 C_{ij}}{\partial r_k \partial r_k}\right)$$

(3)

where $\mathbf{r} = \tilde{\mathbf{x}} - \mathbf{x}$ is the distance between two points in the domain. The pressure velocity correlation is actually closed in this equation. It does not require a model and can be obtained from the equation,

$$\frac{\partial^2 \overline{u_i'p}}{\partial r_j \partial r_j} = -2\overline{u}_{k,j}(\tilde{\mathbf{x}})\frac{\partial C_{ij}}{\partial r_k} - \frac{\partial^2 T_{i(jk)}}{\partial r_j \partial r_k}$$

(4)

Only the triple velocity correlation, $T_{i(jk)}$, representing turbulence-turbulence interactions, requires a model to close Eqn (3). The Reynolds stress tensor (needed to predict the mean flow) is given by $R_{ij}(\mathbf{x}) = C_{ij}(\mathbf{x},0)$.

The reason this equation has not been used as a starting point for practical turbulence models in the past is due to its high dimension. A very coarse discretization of $\mathbf{r}$, with a 10x10x10, mesh implies the need to solve 1000 transport equations for each point in physical space. This cost is too high. A key cost savings comes from recognizing that only very basic information about how the correlations behave in $\mathbf{r}$ is necessary to capture the Reynolds stress evolution (at $\mathbf{r} = 0$) correctly. Our real goal is to model the Reynolds stress evolution accurately, not the two-point correlation. We therefore parameterize the shape of the correlation with the vector parameter, $\mathbf{k}$. and assume that the sum of a few parameterized correlations is sufficient to represent a general correlation function,

$$C_{ij}(\mathbf{x},\mathbf{r}) = \sum \hat{R}_{ij}(\mathbf{x})e^{-|\mathbf{k}\cdot\mathbf{r}|}$$

(5)

Experimental data suggests that an exponential is a good parameterization for the correlation function (Compte-Bellot & S. Corrsin). We have briefly explored the use of other functions and this aspect of the model will be further explored in the proposed work. The model might be considered to be an assumed shape two-point correlation model. It gives roughly the right balance between physical accuracy and computational cost.

Inserting the parameterized two-point correlation (Eqn. 5) into the exact two-point correlation equation (Eqn. 3), and making a similar decomposition for the velocity-pressure correlation, results in the following equations.

$$\hat{R}_{ij,t} = \hat{R}_{jk}\left[2\overline{u}_{l,k}\frac{k_l k_i}{k^2} - \overline{u}_{i,k}\right] + \hat{R}_{ik}\left[2\overline{u}_{l,k}\frac{k_l k_j}{k^2} - \overline{u}_{j,k}\right] - 2\nu k^2 \hat{R}_{ij}$$
$$- \frac{\alpha_H}{\tau}D_{ij} - \left(\hat{R}_{lj}\frac{k_i}{k^2} + \hat{R}_{li}\frac{k_j}{k^2}\right)m_l$$

(6a)

$$k_{i,t} = -k_k\overline{u}_{k,i} - \frac{2}{p+1}\nu k^2 k_i - \frac{1}{p+1}\frac{\alpha_H}{\tau}k_i + m_i$$

(6b)

where $\frac{1}{\tau} = (Kk^2)^{1/2}$ is the inverse turbulence timescale. The terms α_H, D_{ij}, m_l represent the nonlinear turbulence-turbulence interactions and must be modeled.

The models for both D_{ij} and m_l each currently involve one empirical model parameter. However, as a part of the proposed work plan below we have definitive approaches that could reduce the number of empirical model constants to zero for these two terms. The inverse timescale constant α_H was set via DNS data for isotropic decay. It defines the cross over between high and low Reynolds numbers and has very little influence on most predictions (which are at high Reynolds numbers). A good parameterization of the two-point correlation requires a number of these equation systems to be solved (and then summed, Eqn 5). The exact number of systems is a question to be explored in more detail in this project but preliminary results are presented below in the cost section of the proposal.

It has been shown analytically and is demonstrated in some of the figures below that this model gives exact results in the limit of large mean velocity gradients. In addition, the model captures both very low Reynolds number and very high Reynolds number isotropic decay exactly. Isotropic decay depends on nonlinear turbulence-turbulence interactions (the energy cascade). While this process must be modeled, it is notable there are no empirical constants associated with the cascade model in the eddy collision approach.

The OEC model is almost unique in its ability to capture mean flow effects on turbulence exactly. The other two examples of models with this ability are based on the Fourier transform of the Navier-Stokes equations (Reynolds & Kassinos, Van Slooten & Pope). They appear to be strictly limited to homogenous turbulence and periodic domains. The two-point equation (Eqn. 3) and the resulting OEC model are fully general and have no such restrictions.

Detailed Equations

Two main equations are used to represent the oriented collision model. The first one represents $\hat{R}_{ij}$, which is the Reynolds stress (average velocity fluctuations) for one orientation k_i (see equation 7b below). The orientation vector, k_i, has units of 1/length and captures the eddy size and orientation.

$$\hat{R}_{ij,t} = \hat{R}_{jk}\left[\overline{u}_{i,k} + 2\overline{u}^*_{l,k}\left(\frac{k_i k_l}{k^2} - \delta_{il}\right)\right] + \hat{R}_{ik}\left[\overline{u}_{j,k} + 2\overline{u}^*_{l,k}\left(\frac{k_j k_l}{k^2} - \delta_{jl}\right)\right]$$

(7a)

$$-\left(\alpha_L \nu k^2 + \alpha_H \tfrac{1}{\tau_R}\right)\hat{R}_{ij} - \alpha_H\left(\tfrac{1}{\tau_K}\right)D_{ij} - \tfrac{1}{\tau_R}n_i + \left(\hat{R}_{lj}\tfrac{k_i}{k^2} + \hat{R}_{li}\tfrac{k_j}{k^2}\right)m_l + \nabla(\nu + \nu_T)\nabla\hat{R}_{ij}$$

where $\left(\tfrac{1}{\tau_R}\right) = \left(\tfrac{1}{\tau_K}\right) = K^{\frac{1}{2}}\left(\tfrac{N\hat{k}}{K}\right)^{q/2}|k|\left(\tfrac{k}{\hat{k}}\right)^P$. The total Reynolds stress defined as R_{ij} is the averaged sum of the individual $\hat{R}_{ij}$, meaning $R_{ij} = \tfrac{1}{N}\Sigma\hat{R}_{ij}$. Equation (7a) has seven grouped terms. The mean flow gradients and system rotation is accounted for by $\overline{u}^*_{i,k} = \overline{u}_{i,k} + e_{ikj}\Omega_k$,

with Ω_k being the rotation vector for a non-inertial frame. The dissipative behavior of the model is captured by $\left(\alpha_L \nu k^2 + \alpha_H \frac{1}{\tau_R}\right)\hat{R}_{ij}$ and $\alpha_H \left(\widehat{\frac{1}{\tau_R}}\right)D_{ij}$ is the return-to-isotropy model discussed in section 3.3 below. The factor $\left(\widehat{\frac{1}{\tau_R}}\right)$ is the timescale used to model the dissipation. $\frac{1}{\tau_R}n_i$ is the rotation term. The six term $\left(\hat{R}_{lj}\frac{k_i}{k^2} + \hat{R}_{li}\frac{k_j}{k^2}\right)m_l$ arises from the need to maintain orthogonality ($R_{ij}k_i = 0$) between the orientations and the $\hat{R}_{ij}$ (m_l is the k-return model). Incompressibility requires $R_{ij}k_i = 0$. The final term $\nabla(\nu + \nu_T)\nabla\hat{R}_{ij}$ models the diffusive action of the Reynolds stresses.

The second equation represents the orientation k_i with its time-derivative defined as:

$$k_{i,t} = -k_k\bar{u}_{k,i} - \frac{1}{l}(\alpha_L \nu k^2 + \alpha_H \frac{1}{\tau_R})k_i + \frac{1}{\tau_R}n_i + \left(\widehat{\frac{1}{\tau_R}}\right)m_i + \nabla(\nu + \nu_T)\nabla k_i \qquad (7b)$$

The above equation contains six grouped terms. The first terms captures the mean gradient effects (shear). This term is the equation for passive disks. Just as in (2.3.1), the second term captures the dissipation; l takes on the value 3 or 5 respectively for the $\hat{k}^2$ or $\hat{k}^4$ low wave number. The third term n_i present in $\frac{1}{\tau_R}n_i$ models the secondary rotation effects and m_i is the return model for the orientations. The last term, $\nabla(\nu + \nu_T)\nabla k_i$ accounts for the diffusive action of the orientation vectors k_i.

In addition,

$$K_{,t} = \sum \hat{R}_{ik}\left[\bar{u}_{i,k} - 2\bar{u}_{i,k}^{\cdot}\right] - \alpha_L \nu \sum k^2\hat{K} - \alpha_H \sum \left(\widehat{\frac{1}{\tau_R}}\right)D_{ij} \qquad (8)$$

Hence,

$$\varepsilon = \alpha_L \nu \sum k^2\hat{K} + \alpha_H \sum \left(\widehat{\frac{1}{\tau_R}}\right)D_{ii} \qquad (9)$$

Ability to Represent Two-point Correlations

The unknowns in the oriented eddy model are closely related to the two-point correlations. In this section, we take a brief look at this relationship. Assume $R_{ij}(\vec{x}, \vec{r}) \approx \sum \hat{R}_{ij} F(\vec{k} \cdot \vec{r})$ where $F(\eta)$ is a simple function of $\vec{r}$, the distance between two points. Considering the specific case where $F(\vec{k}, \vec{r}) = e^{-|\vec{k}\cdot\vec{r}|}$, then $R_{ij}(\vec{x}, \vec{r}) = \sum \hat{R}_{ij}e^{-|\vec{k}\cdot\vec{r}|}$. When looking at the two point correlation in the x-direction for example, we get
$$R_{11}(r_1, r_2, r_3) \approx \sum \hat{R}_{11}e^{-|k_1 r_1 + k_2 r_2 + k_3 r_3|}$$
Similarly for R22 and R33:
$$R_{22}(r_1, r_2, r_3) \approx \sum \hat{R}_{22}e^{-|k_1 r_1 + k_2 r_2 + k_3 r_3|}$$
$$R_{33}(r_1, r_2, r_3) \approx \sum \hat{R}_{33}e^{-|k_1 r_1 + k_2 r_2 + k_3 r_3|}$$

Hence, we obtained the contour plots shown below that look very similar to the two-point correlations found from DNS data.
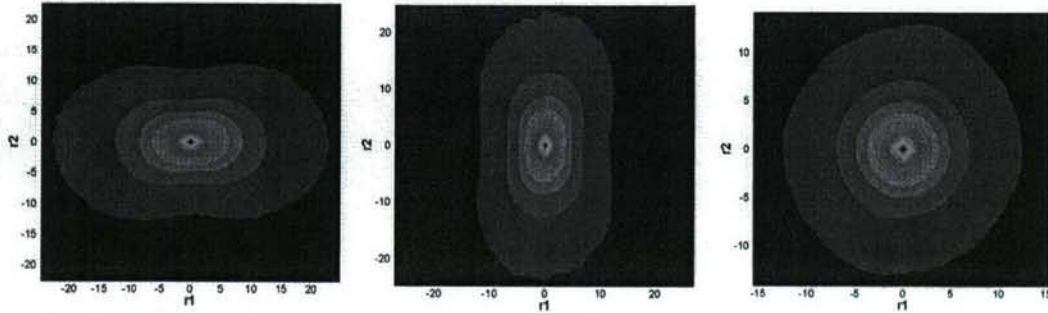

Figure 3. R_{11}, R_{22} and R_{33} as seen from the r_3-direction.

DNS two-point correlation data corresponding to the first two figures above (the model) is shown below in Figure 4. The shapes are very similar. The mesh size used in the DNS simulation was 768 by 768 by 1536 cells, with a domain size of 56.54 by 56.54 by 113.09 centimeters.
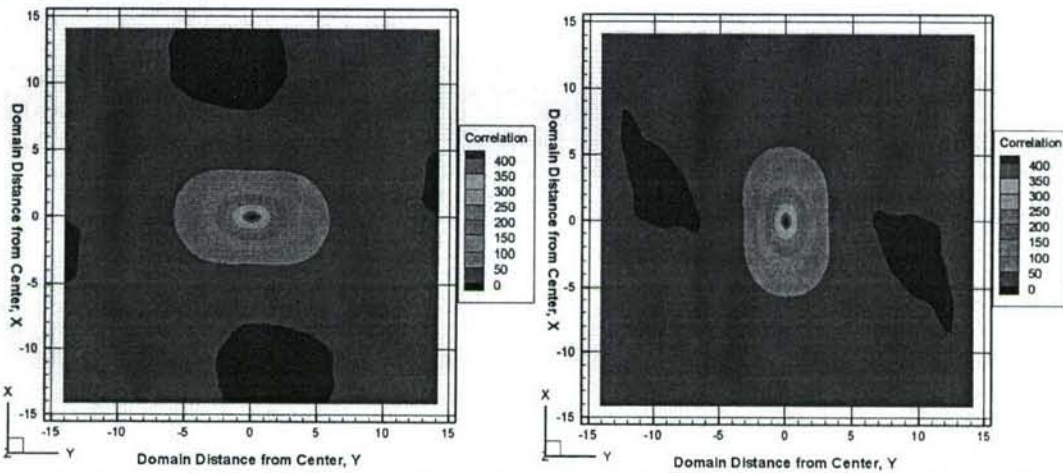

Figure 4. A planar slice of a three dimensional R_{11} and R_{22} two-point correlation in the X-Y plane about Z=0.

A major break through of the current modeling approach is the ability to model the 'blocking' affect of walls exactly. After a vertical wall is inserted (at y = -2 in the figures above) the two-point correlations are dramatically altered. This is shown in figure 5.

10
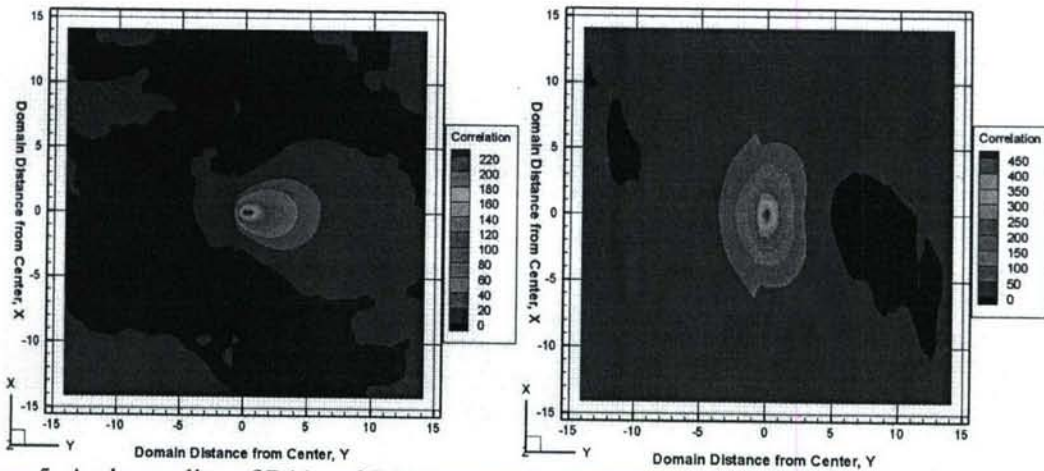
Figure 5. A planar slice of R11 and R22 two-point correlations in the X-Y plane about Z=0 after a wall is inserted at y=-2.

The essence of the exact wall representation is shown in figure 6 for the R_{22} correlation This correlation is chosen to illustrate the idea because it is the most dramatically altered correlation. In the figure below, the red is DNS data and the blue is the model. This figure is the R_{22} correlation along a line perpendicular to the wall. Only results to the right of y=-2 matter. To the left of y=-2 there is now a solid wall. The model uses image eddies to exactly capture the influence of the wall on the two-point correlations.
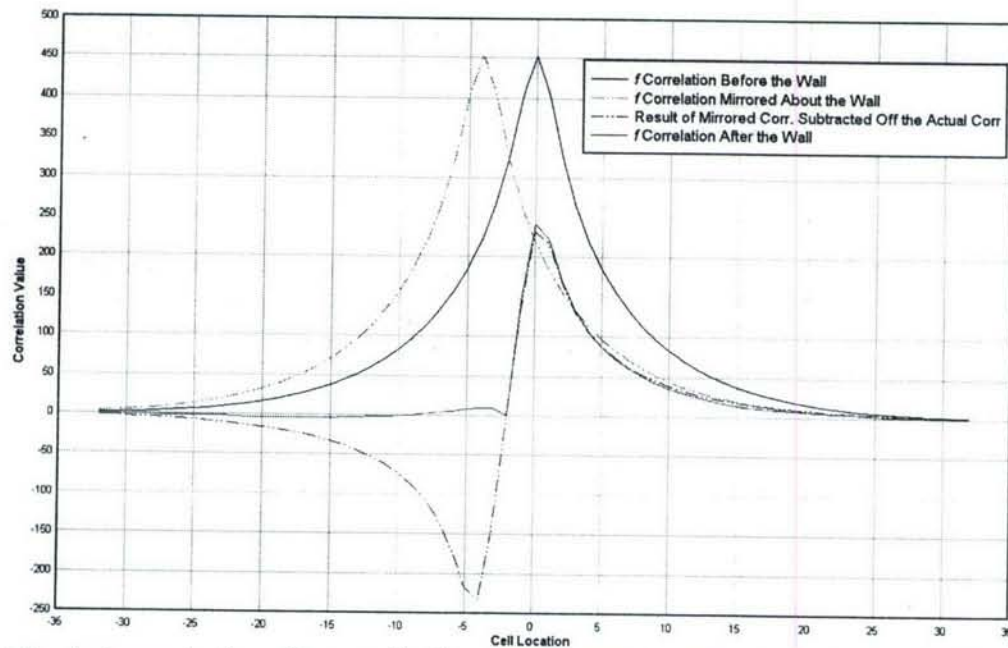
Figure 6. A demonstration of how wall effects can be exactly captured by the eddy OEC model.

NUMERICAL RESULTS

Below is the table that summarizes the different sections and results of the current project
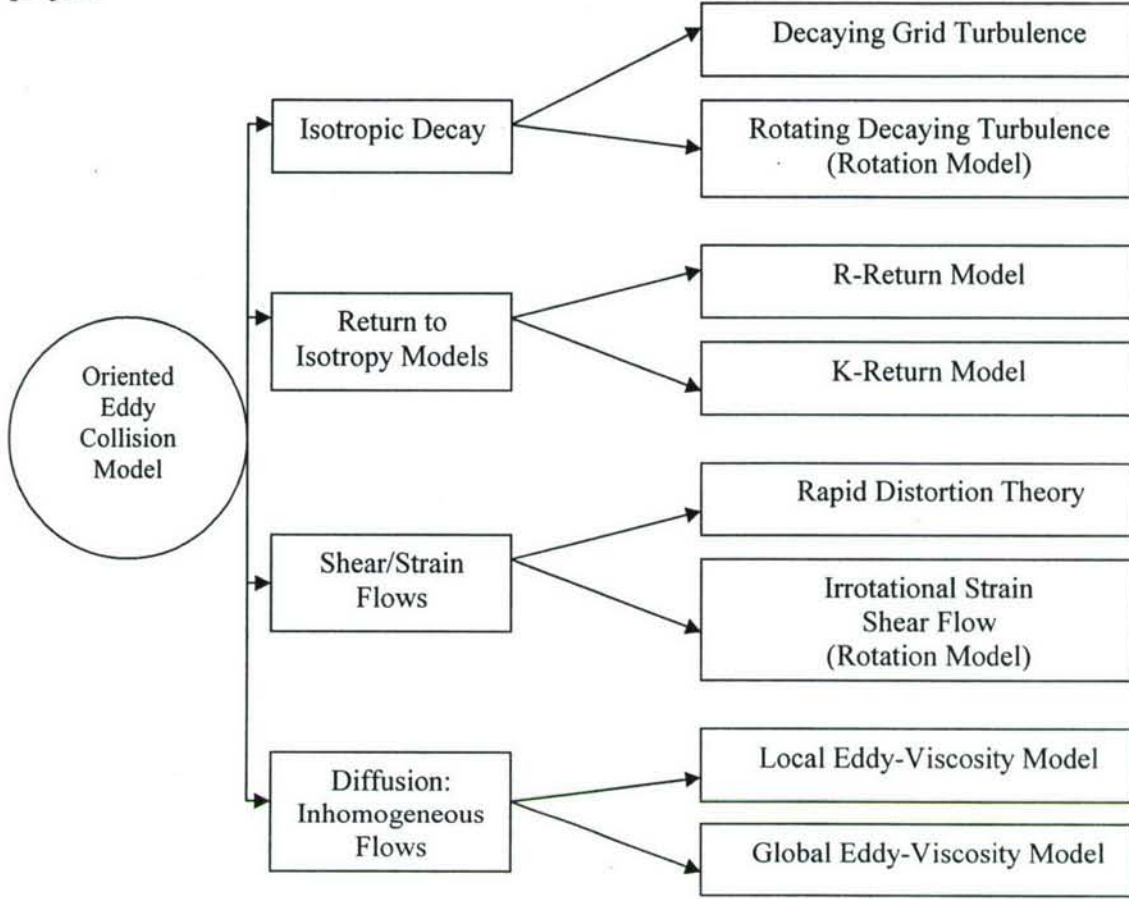
Table 1. Research Summary

1. Isotropic Decay

In general, when the properties of a material are the same in all directions, the material is said to be isotropic. In the case of turbulence, if the fluctuations are independent of direction, the turbulence is isotropic. When the fluctuations do not have any directional preference, then the off-diagonal components of R_{ij} vanish, and $R_{11} = R_{22} = R_{33}$. Mathematically, this corresponds to $R_{ij} = \frac{2}{3} K \, \delta_{ij}$.

In this work, it is necessary to define isotropy for the orientations as well. For isotropy, all orientation vectors have the same magnitude and are uniformly distributed on the sphere.

Von Karman & Howarth first suggested in 1938 that the decaying turbulence should have a power law behavior of the form:

$$K = K_0 \left(1 + \frac{\varepsilon_0 t}{nK_0}\right)^{-n}$$

(10)

where K_0 is the initial turbulent kinetic energy and ε_0 represents the initial dissipation, and n is the decay exponent. While all researchers agree on the power law form, there is less agreement on what the value for n should be. However, most investigators agree that the exponent n is highly dependent on the low wavenumber $\hat{k}$ of the energy spectrum (Saffman). In the case where the low wavenumber portion of the spectrum goes as $\hat{k}^2$, n corresponds to 3/2 at low Reynolds number and 6/5 at high Reynolds number. On the other hand, when the low wavenumber portion of the spectrum goes as $\hat{k}^4$, n corresponds to 5/2 for low Reynolds number and 10/7 for high Reynolds number.

We will attempt to obtain all these limits with the OEC model. For isotropic decaying turbulence, the dissipation ε is,

$$\varepsilon = -\frac{dK}{dt}$$

(11)

Substituting, equation (3.1.1.1) to (3.1.1.2) above, we obtain:

$$\varepsilon = \varepsilon_0 \left(1 + \frac{\varepsilon_0 t}{nK_0}\right)^{-n-1}$$

(12)

In this section, our model attempts to capture the evolution of n as a function of the turbulent Reynolds number ($Re_T = \frac{K^2}{\nu\varepsilon}$, with ν being the fluid kinematic viscosity) for low wavenumber (not orientations) of $\hat{k}^2$ and $\hat{k}^4$. Figure 4 below summarizes the results obtained when the low wavenumber behavior of the spectrum is $\hat{k}^2$.
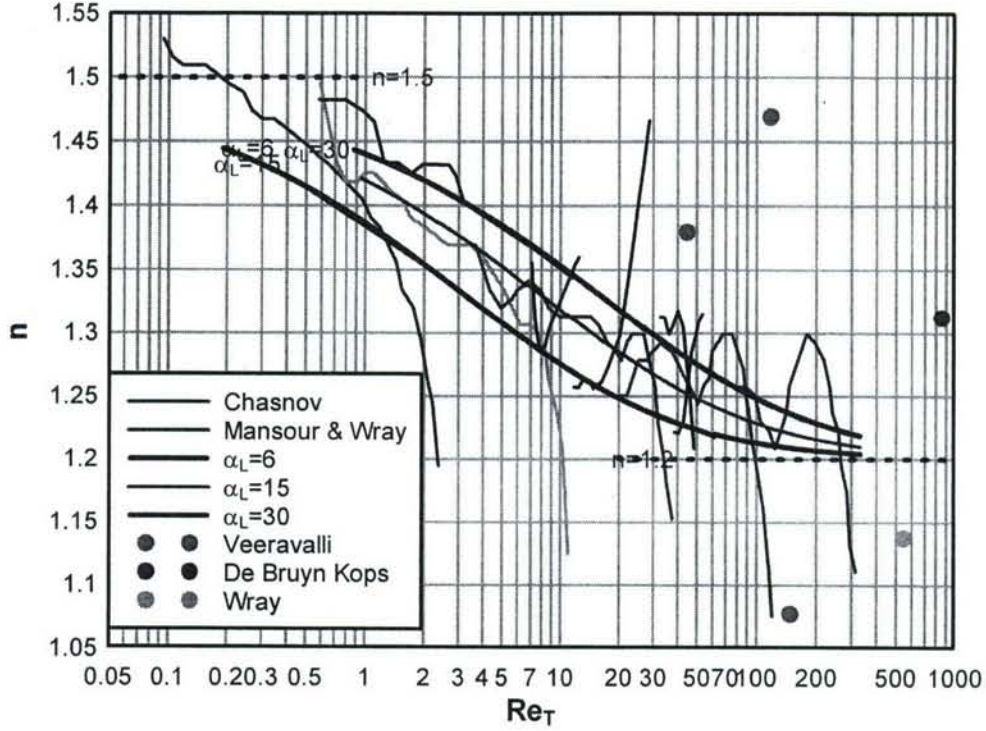
Figure 7: Power-law exponent as a function of the turbulent Reynolds number for a $\hat{k}^2$ low wavenumber spectrum.

The thick maroon and dark green lines represents the model predictions ($\alpha_L = 6, 15, 30$ for $\alpha_H = 1$). For our purpose, we determined that the ratio $\dfrac{\alpha_L}{\alpha_H} = 15$ (maroon curve) best matched the DNS simulations of Chasnov, Mansour & Wray. The upper and lower purple dashed lines included in the figure are the low and high Reynolds bounds on n. Notice that the model obtains these limits independent of α_L. Also on Figure 7 are shown the exponent values for the DNS of de Bruyn Kops.

When the low wavenumber behavior of the spectrum goes as $\hat{k}^4$, we obtained the results shown in Figure 8 below. Again, the horizontal green dash lines represent the upper (5/2) and lower (10/7) limits of the exponent for $\hat{k}^4$ spectrum. The thick purple and blue lines are the model predictions for $\dfrac{\lambda_L}{\lambda_H} = 10, 25, 50$. In addition to these curves, there are four 128^3 DNS simulations by Yu et al. and four 256^3 DNS simulations by Mansour & Wray. For the same reason mentioned above, we determined that $\dfrac{\lambda_L}{\lambda_H} = 15$ (not shown) is an adequate compromise. Note that this ratio is similar to the one determined above for $\hat{k}^2$.
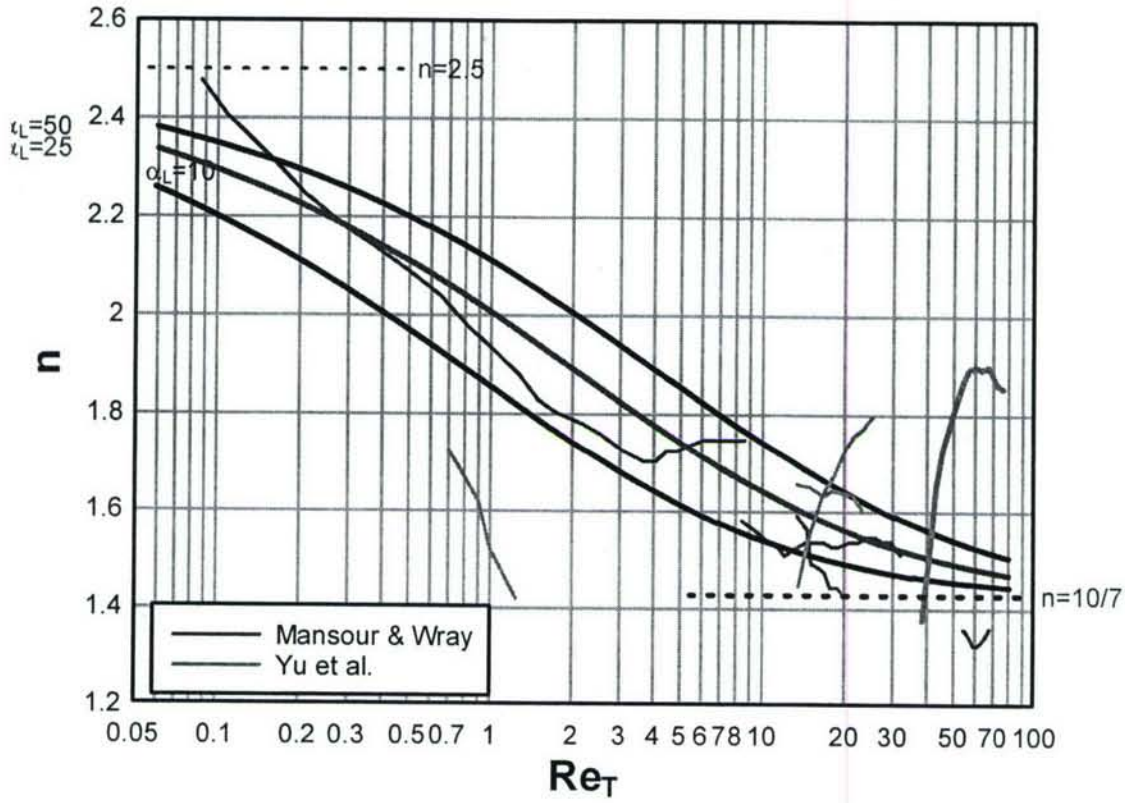
14

Figure 8. Power law exponent as a function of Reynolds number for a $\hat{k}^4$ low wavenumber spectrum.

Kinetic Energy

In this section, we focus our efforts on predicting the decay of kinetic energy in isotropic flows (other than just the exponent). This is essentially a posteriori test of the chosen value $\dfrac{\lambda_L}{\lambda_H} = 15$. We test the model against numerous published data: some experimental, some LES and other DNS. In determining the kinetic energy, the equations used in our model predictions originate from equation (7a) and (7b) above with the particularity that the flow is isotropic. Hence, there is no need to include the return-to-isotropy ($D_{ij} = 0$) as well as the diffusion terms: $\nabla(\nu + \nu_T)\nabla\hat{R}_{ij} = 0$, $\nabla(\nu + \nu_T)\nabla k_i = 0$. Thus, in cases where no rotation is present,

$$\hat{R}_{ij,t} = -\left(15\nu k^2 + \tfrac{1}{\tau_R}\right)\hat{R}_{ij} \tag{13a}$$

$$k_{i,t} = -\frac{1}{l}(15\nu k^2 + \tfrac{1}{\tau_R})k_i \tag{13b}$$

where $l = 3$ for k^2 and $l = 5$ for k^4 low wavenumber spectra.

15

Data and model predictions are shown below for low and intermediate turbulent Reynolds numbers. In addition, we state all initial conditions in Table 2 below:

	Wigeland & Nagib (exp. Data)			Mansour, Cambon & Speziale (DNS)		Jacquin (exp. Data)			de Bruyn Kops (DNS)	Squires (LES)	
$\varepsilon(m^2/s^3)$	14.85	2.96	2.77	0.93	0.95	11.73	16.43	30.93	0.782	1.27	1.35
$K(m^2/s^2)$	0.098	0.045	0.029	0.964	0.977	0.15	0.264	0.462	0.087	0.265	0.298
$v(m^2/s)$	1.8 e-5	1.8 e-5	1.8 e-5	3.67 e-2	1.49 e-2	1.51 e-5	1.51 e-5	1.51 e-5	1.49 e-5	8.6 e-5	8.6 e-5
Re_T	36	38	17	27.2	67.1	127	281	457	655	643	764

Table2. Initial conditions

In Figure 9, the kinetic energy is represented versus time. The asterisks, the triangles and the stars correspond to the experimental data with corresponding Re_T=36, 38 and 17 while the dashed lines correspond to our simulations.
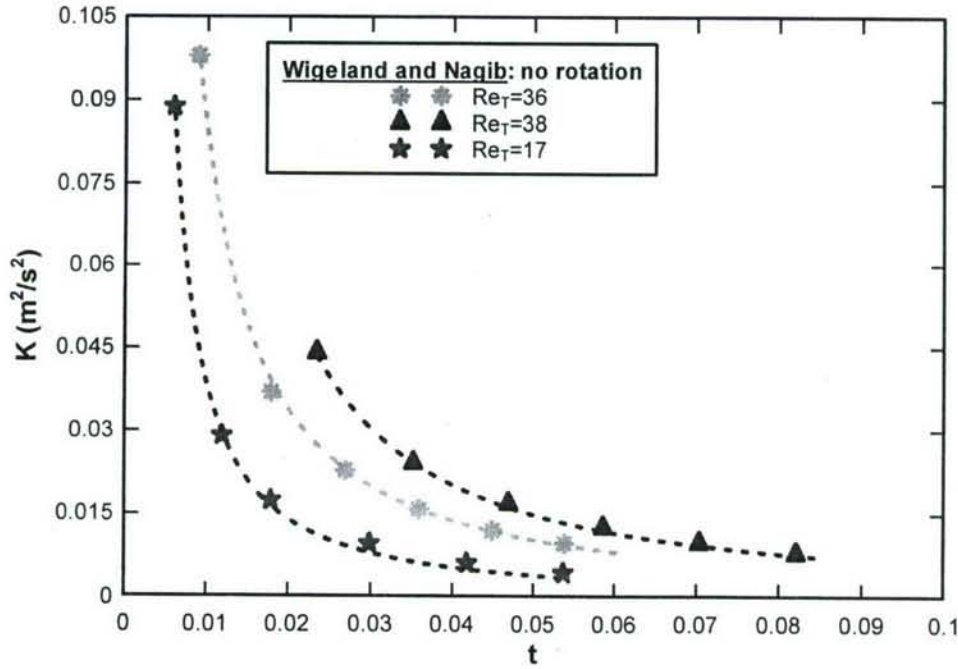
Figure 9. Wigeland and Nagib's decaying kinetic energy.

In Figure 10, the kinetic energy versus time is shown. The orange dots correspond to the experimental data for Re_T=27.24 and the purple ones are for Re_T=67.1. The solid lines correspond to our simulations. Clearly, the OEC model shows good agreement with the DNS data of Mansour, Cambon and Speziale.
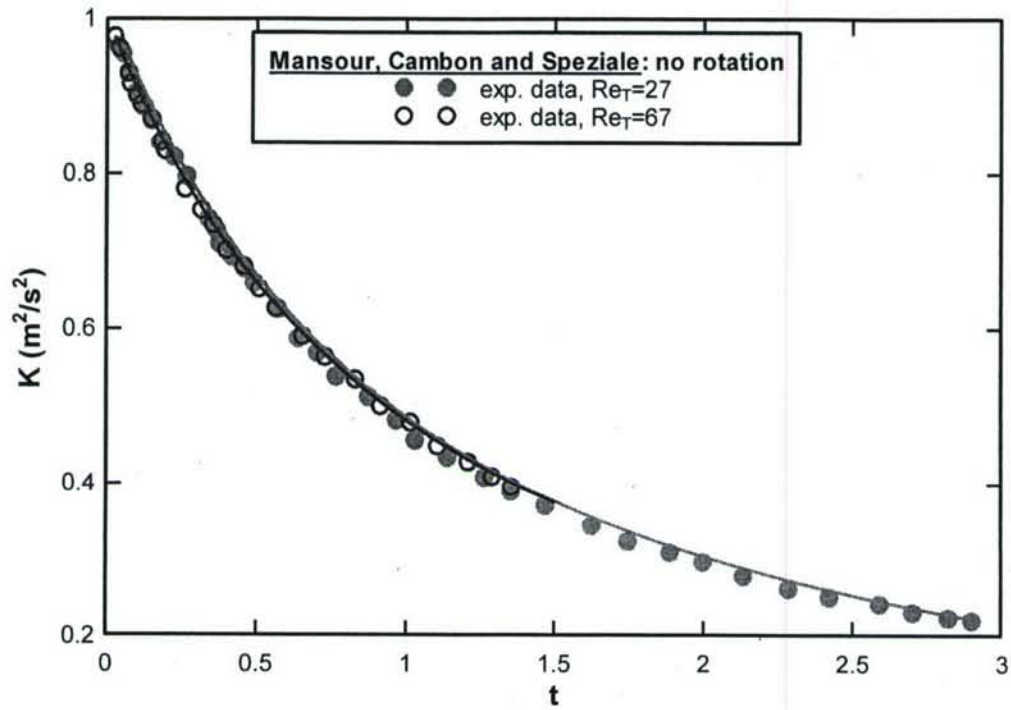
Figure 10. Mansour, Cambon and Speziale's decaying kinetic energy.

Figure 11 shows the kinetic energy versus time. The asterisks correspond to the experimental data and the dashed lines correspond to the simulations.
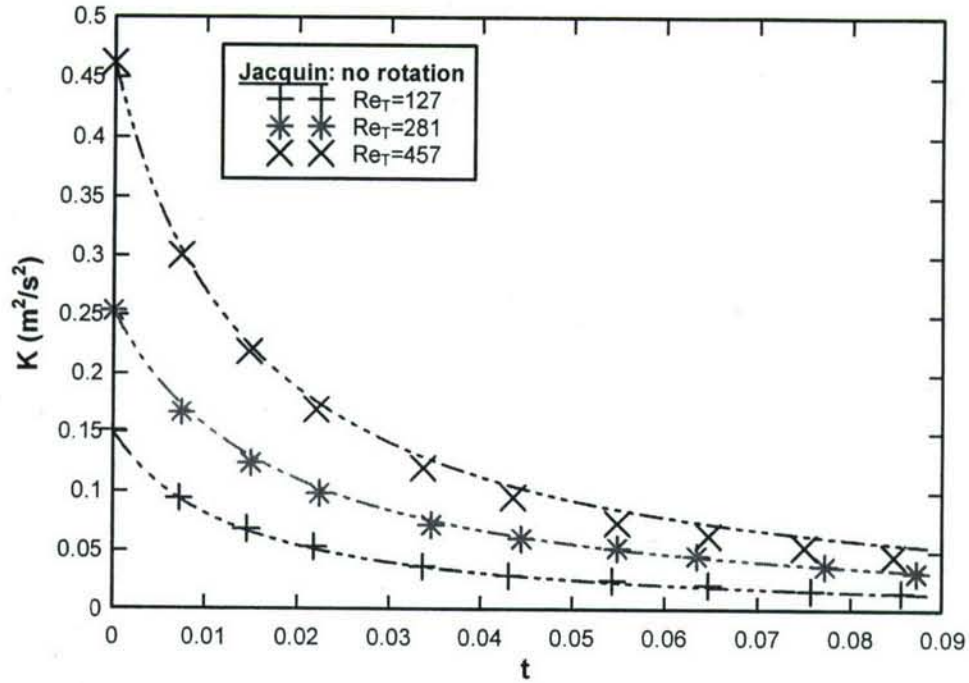
Figure 11. Jacquin's decaying kinetic energy.

Figure 12 shows the kinetic energy versus time. The red asterisks correspond to DNS data of de Bruyn Kops for $Re_T=655$ and the dashed lines correspond to the oriented eddy model simulations.
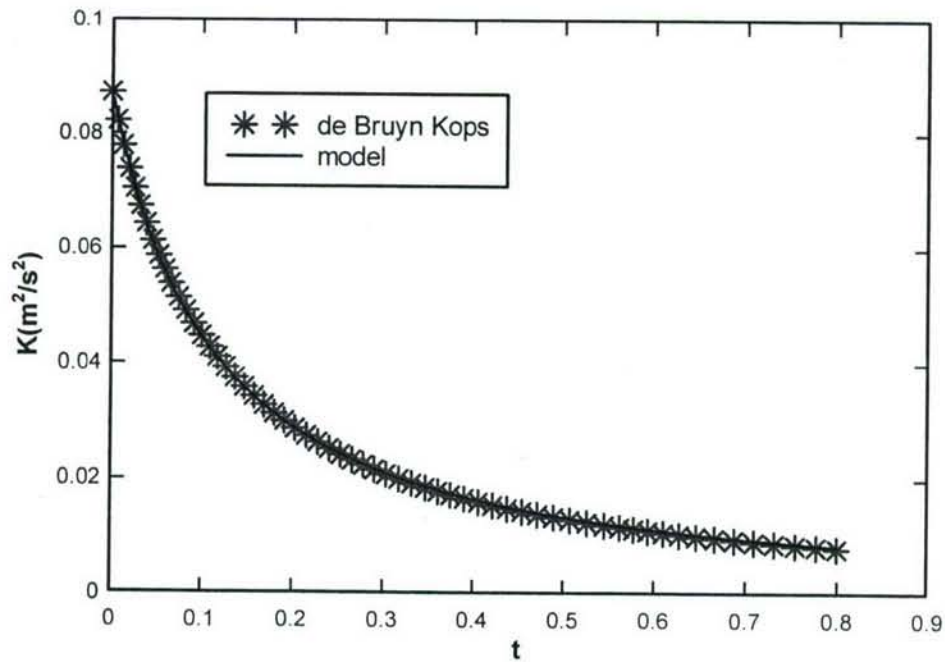

Figure 12. de Bruyn Kops's decaying kinetic energy.

Figure 13 shows the kinetic energy versus time. The green asterisks correspond to the $\hat{k}^2$ experimental data with $\mathrm{Re}_T = 643$. The red asterisks represent $\hat{k}^4$ data with $\mathrm{Re}_T = 764$. The blue and pink lines correspond to our simulations.
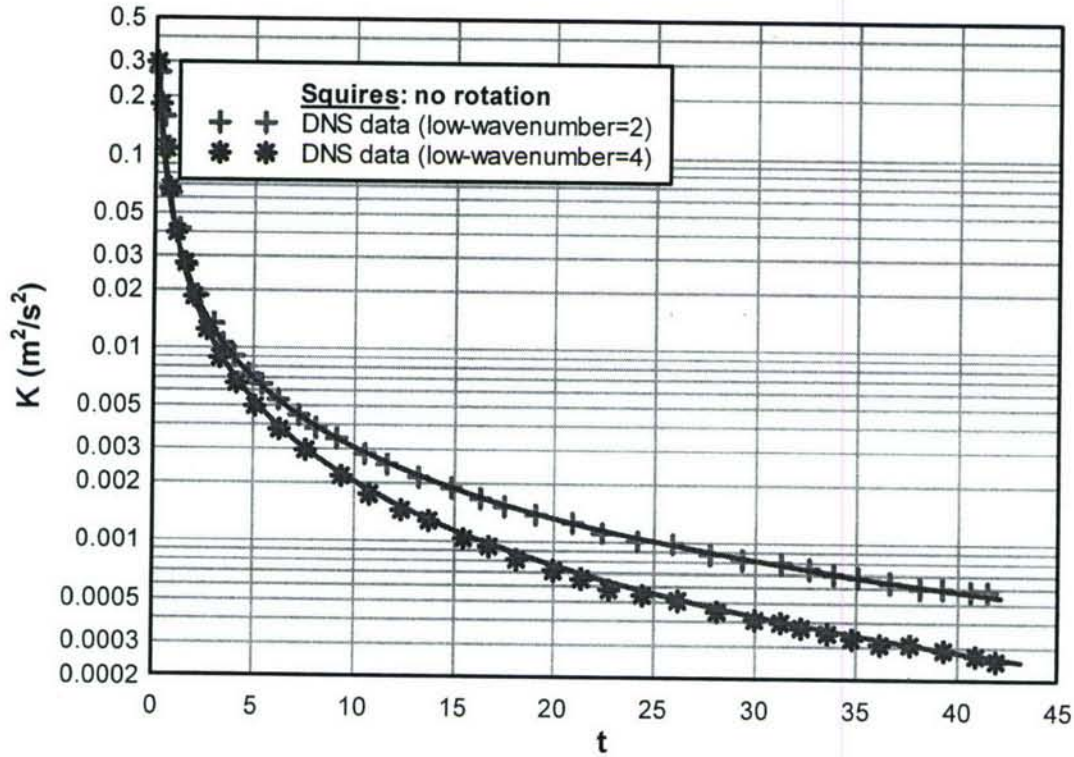
Figure 13. Squires' decaying kinetic energy for both $\hat{k}^2$ and $\hat{k}^4$.

Based on the data presented above, it is concluded that the OEC model performs well in predicting the decaying kinetic energy for simple (homogeneous, isotropic and irrotational) turbulent flows.

Rotating Decaying Grid-Turbulence

To measure the degree of rotation present in the flow, we used a turbulent Rossby number defined as follow:

$$Ro_T = \frac{\varepsilon}{K\Omega^\bullet} \tag{14}$$

Large Ro_T means no rotation, whereas $Ro_T < 1$ implies a flow dominated by rotation. With rotation present, the model equations become:

$$k_{i,t} = -\tfrac{1}{3}(15\nu k^2 + \tfrac{1}{\tau_R})k_i - \tfrac{1}{\tau_R}n_i \tag{15}$$

Three models for the rotation term were tested:

$$n_i^A = \frac{\left|\vec{k}\cdot\vec{\Omega}^*\right|}{(C_1 k^2 K^{\frac{1}{2}} + C_2 |k||\Omega^*|)}k_i$$

or

$$n_i^B = \frac{(\vec{k}\cdot\vec{\Omega}^*)}{(C_1 k^2 K + C_2 (\vec{\Omega}^*)^2)}\Omega_i^* \tag{16}$$

or

$$n_i^C = \frac{(\vec{k}\cdot\vec{\Omega}^*)^2/k^2}{(C_1 k^2 K + C_2 (\vec{\Omega}^*)^2)}k_i$$

where $\Omega_i^* = \varepsilon_{ijk}U_{k,j} + \Omega_i^{\text{frame}}$. In earlier work Chartrand briefly looked at the first two models, n_i^A and n_i^B. However, after extensively studying the performance of each of these models and comparing them to multiple DNS results, we came to the conclusion that the above two terms each only captures a different aspect of the rotation. Hence, the third model was developed.

With each model, come two constants C_1 and C_2 that are used to tune the model behavior. That is, C_1 and C_2 are both model-dependent. From equations (3.1.3.3) above, it is clear that C_2 affects simulations at large rotation rates while C_1 acts at small rotation rates. We used this concept in determining the values for both C_1 and C_2. Table 3 below summarizes the values:

Model	Formula	C_1	C_2
k	$\dfrac{\left|\vec{k}\cdot\vec{\Omega}^*\right|}{(C_1 k^2 K^{\frac{1}{2}} + C_2 |k||\Omega^*|)}k_i$	8	0.25
Ω	$\dfrac{(\vec{k}\cdot\vec{\Omega}^*)}{(C_1 k^2 K + C_2 (\vec{\Omega}^*)^2)}\Omega_i^*$	20	¼
Smooth k	$\dfrac{(\vec{k}\cdot\vec{\Omega}^*)^2/k^2}{(C_1 k^2 K + C_2 (\vec{\Omega}^*)^2)}k_i$	20	¼

Table 3: Rotation-models along with their respective tuning constants C_1 and C_2

Next, we compared the performance of each model for three sets of data: Jacquin, Mansour Cambon & Speziale, and Blaisdell. The *k-smooth* model outperforms the other two. The initial conditions are shown in Tables 4, 5 and 6 below:

	Mansour, Cambon & Speziale				Jacquin			Blaisdell
$\varepsilon(m^2/s^3)$	0.93		0.95		11.73	16.43	30.93	1.78
$K(m^2/s^2)$	0.964		0.977		0.153	0.288	0.444	1
$v(m^2/s)$	3.67e-2		1.49e-2		1.51e-5	1.51e-5	1.51e-5	4.41e-2
Re_T	27.2		67.1		127	281	457	12.75
Ro_T	0.37	0.037	0.24	0.1	1.22	0.91	1.10	---
S	---	---	---	---	---	---	---	3

Table 4: Initial conditions of Mansour, Cambon & Speziale, Jacquin and Blaisdell.

	Wigeland & Nagib					
$\varepsilon(m^2/s^3)$	14.67	14.94	3.49	3.36	3.36	22.26
$K(m^2/s^2)$	0.0975	0.105	0.0462	0.051	0.033	0.096
$v(m^2/s)$	1.8e-5	1.8e-5	1.8e-5	1.8e-5	1.8e-5	1.8e-5
Re_T	36	41	34	43	18	23
Ro_T	7.52	1.78	3.77	0.82	5.09	2.9

Table 5: Wigeland & Nagib's initial conditions.

	Shimomura			de Bruyn Kops	Veeravalli	
$\varepsilon(m^2/s^3)$	0.024	0.025	0.028	0.0992	7.96	8.13
$K(m^2/s^2)$	0.098	0.2619	0.5638	5.888e-2	0.17	0.202
$v(m^2/s)$	8.0e-3	8.0e-3	8.0e-3	1.4854e-5	1.6e-5	1.6e-5
Re_T	50	343	1419	2353	227	313
Ro_T	N/A	0.095	0.017	0.006	0.5	0.32

Table 6: Initial conditions of Shimomura, de Bruyn Kops and Veeravalli.

In Figure 14 below, the performance of each model is analyzed using the DNS data from Jacquin. Our simulation matched the dimensionless initial conditions of Jacquin as represented in Table 4. The crosses, stars and dots represent the experimental data. The solid lines represent ω, the dashed lines k and the dotted lines *k-smooth*.
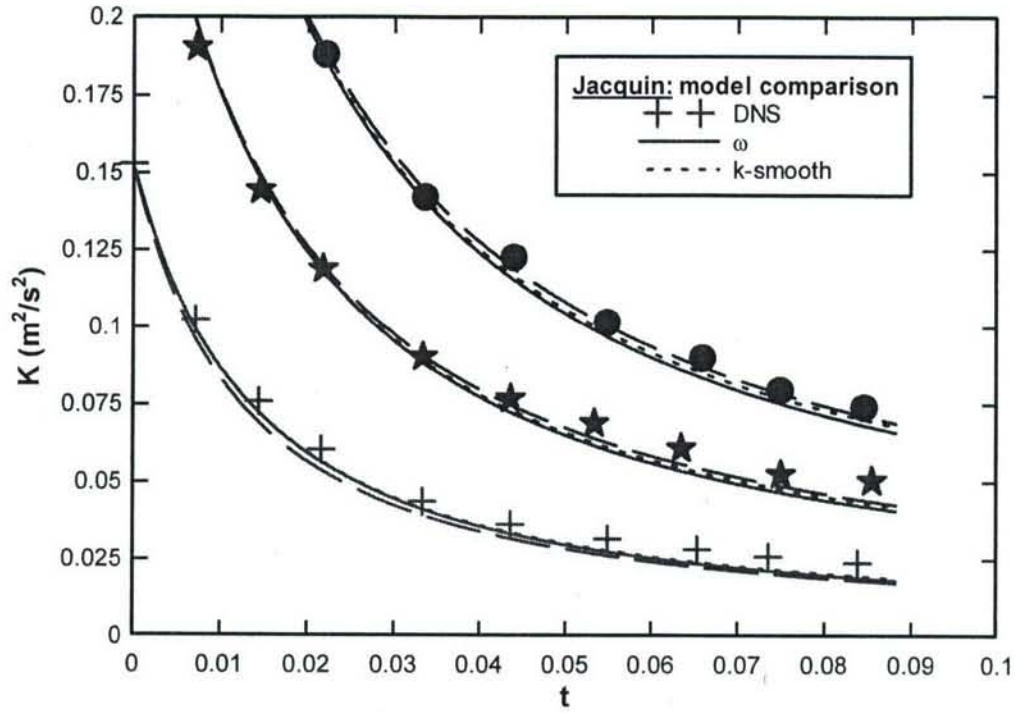
Figure 14: Performance comparison of k, ω and *k-smooth* rotation terms.

Looking at the graph above, it is concluded that all three rotation models performed equally in this case, due to the somewhat identical turbulent Rossby numbers (1.22, 0.91 and 1.10).

In Figure 15, the dimensionless initial conditions of Mansour, Cambon & Speziale were matched for Re_T=27.24.
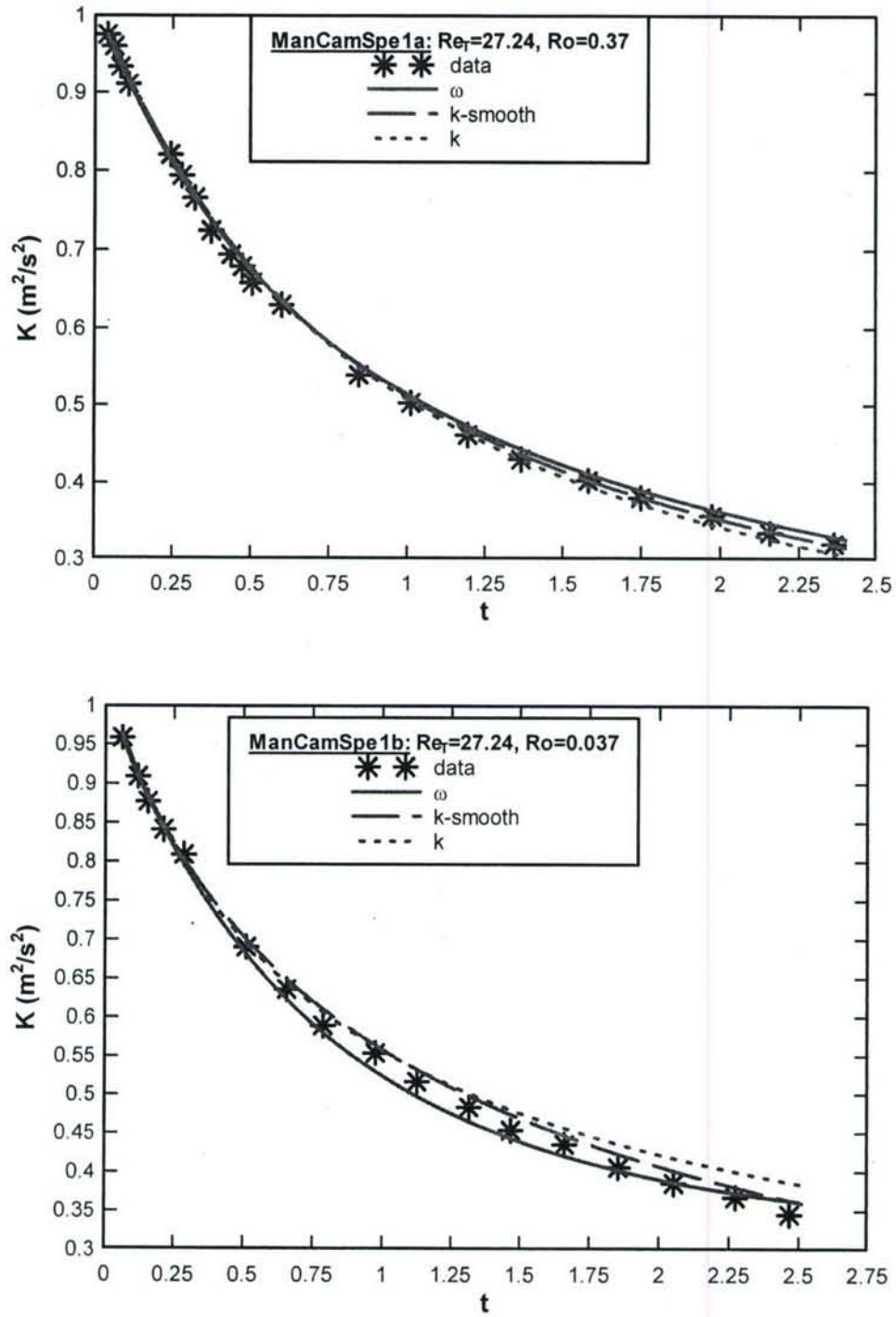

Figure 15. Performance comparison of k, ω and k-$smooth$ rotation terms based on Mansour, Cambon and Speziale experimental data. a) Ro=0.37. b) Ro=0.037.

In Figure 16, the dimensionless initial conditions of Mansour, Cambon & Speziale were matched for Re_T=67.1.
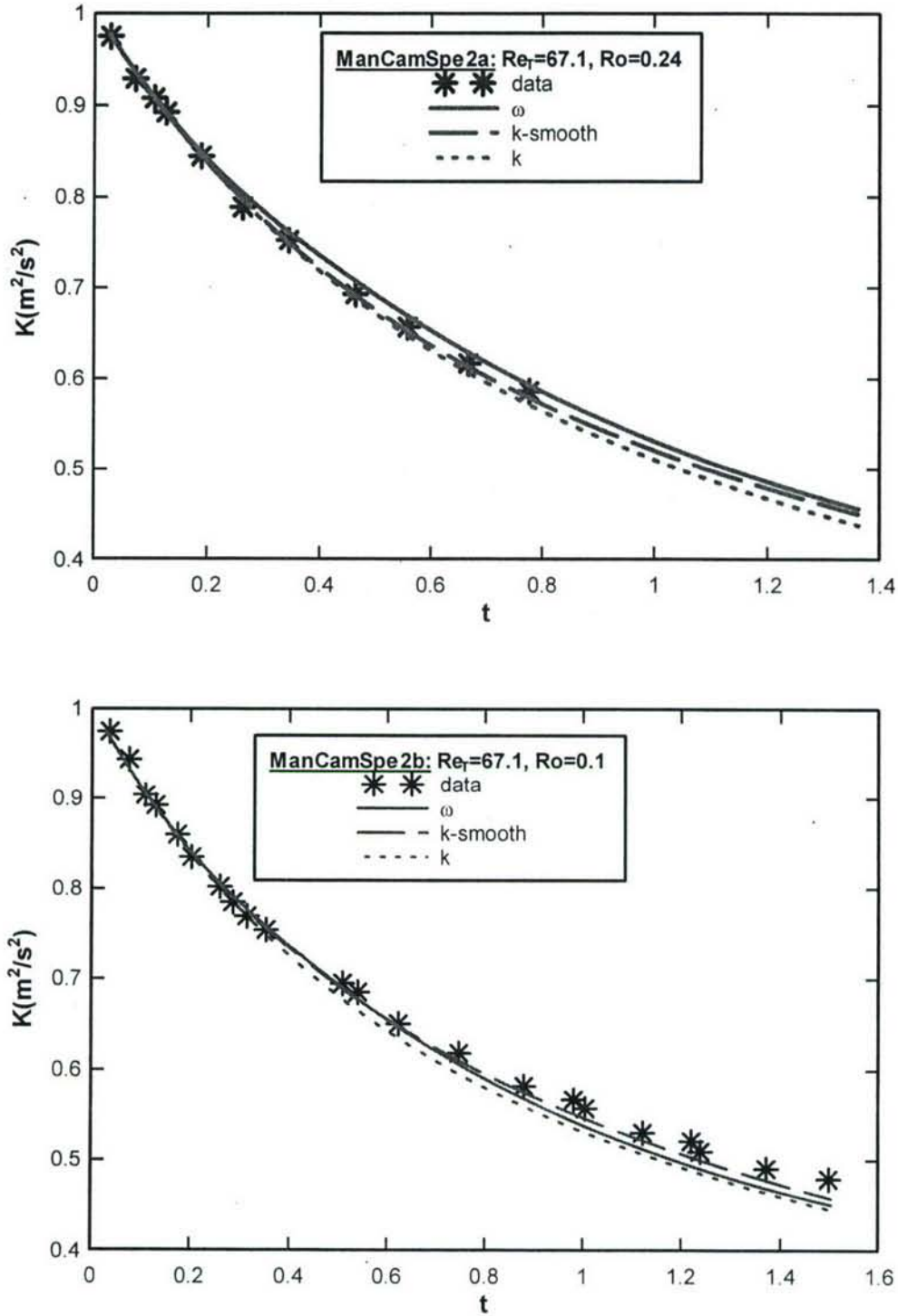
Figure 16: Performance comparison of k, ω and *k-smooth* rotation terms based on Mansour, Cambon and Speziale's experimental data. a) Ro=0.24. b) Ro=0.1.

We also evaluated all three rotational models for homogeneous flows; specifically, using data from Blaisdell's elliptical flow as shown below in Figure 17:
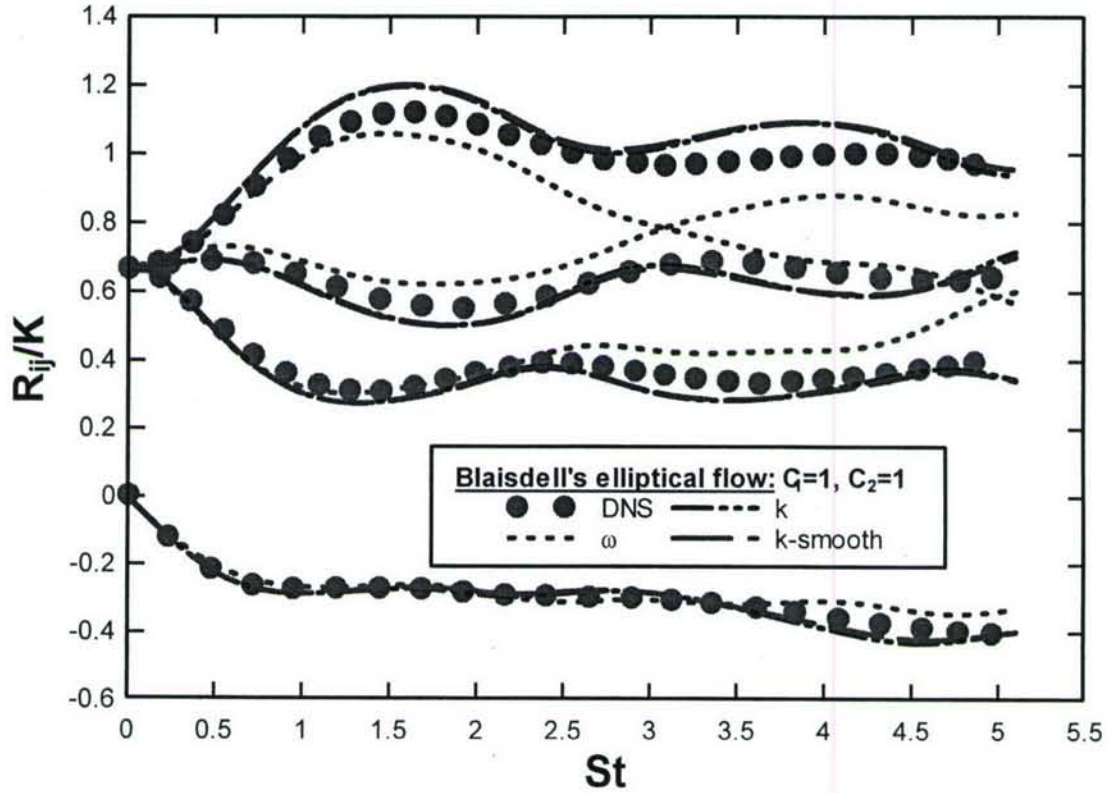
Figure 17: Performance comparison of *k*, *ω* and *k-smooth* rotation terms for Blaisdell. (homogeneous shear flow)

From the graphs above, the k-*smooth model* is always consistently between the *k* and the *ω-models*. And sometimes the difference is so subtle that it is almost negligible. In the Blaisdell case however, the w *ω-model* performs very poorly. Hence, it was decided that the *k-smooth model* performs the best. So, the OEC model was tested against other published data such as Wigeland &Nagib, Jacquin, Shimomura, de Bruyn Kops, Veeravalli and Mansour, Cambon and Speziale. (The initial conditions are presented in Tables 5 and 6 above). The non-rotating initial conditions for Wigeland & Nagib as well as de Bruyn Kops were already given above in the prior section on decaying turbulence.

In Figure 18 below, the asterisks, triangles and stars represent the experimental data of Wigeland & Nagib for low Reynolds number, while the dotted lines represent the predictions for the collision model.
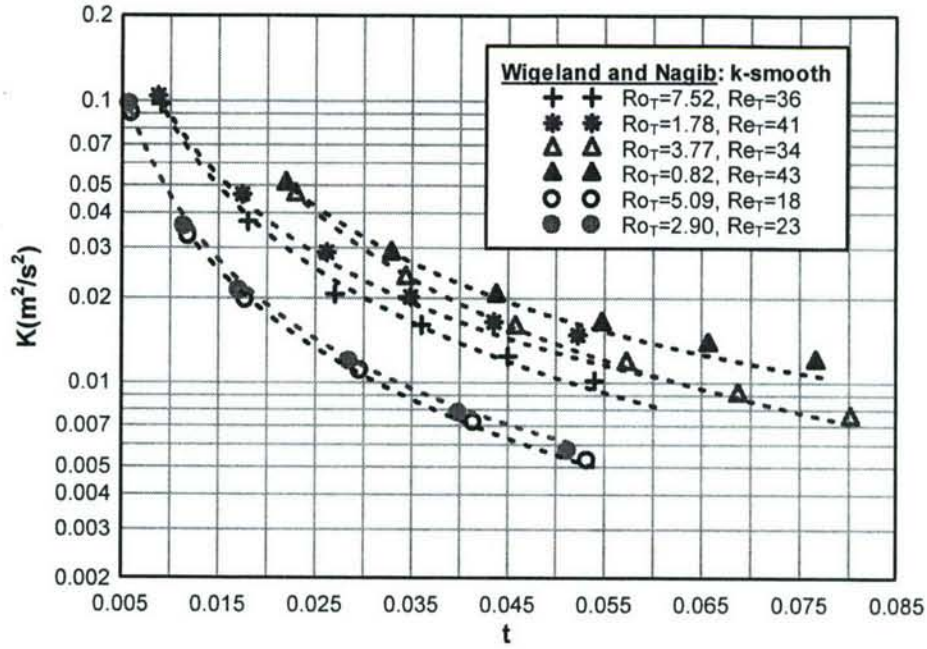
Figure 18: Rotating isotropic decay of Wigeland & Nagib using the rotation model n_i^C.
Turbulent kinetic energy versus time.

In Figure 19, the asterisks, crosses and squares represent the experimental data of Jacquin, while the dashed lines represent the predictions of the collision model with n_i^C for rotation model. The numbers in parenthesis 140, 310 and 500 correspond to the turbulent Reynolds number.
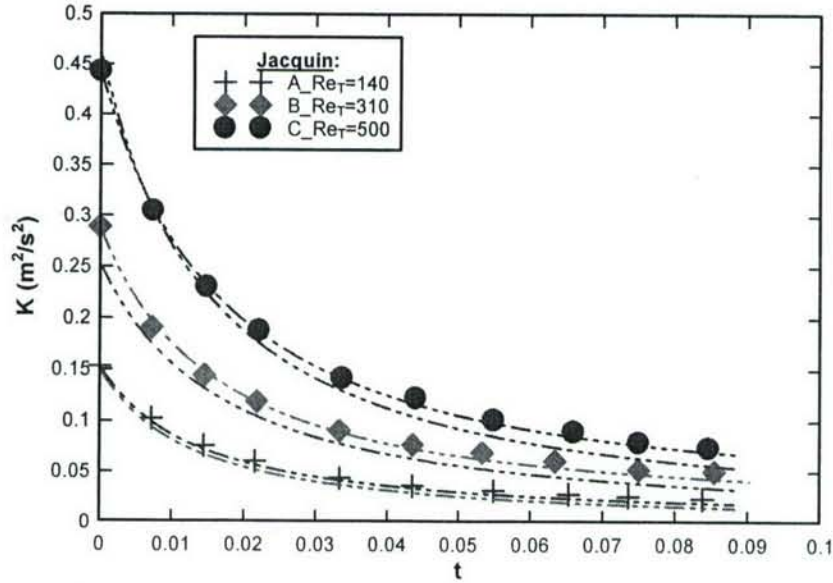

Figure 19: Rotating Isotropic decay of Jacquin. Turbulent kinetic energy versus time.

In Figure 20, the asterisks represent the experimental data of Shimomura (for both irrotational and rotational cases), while the solid lines represent the predictions from our collision model. As summarized in Table 6 above, the turbulent Reynolds numbers correspond respectively to 50, 343 and 1419. In addition, the data sets are for $\hat{k}^2$.
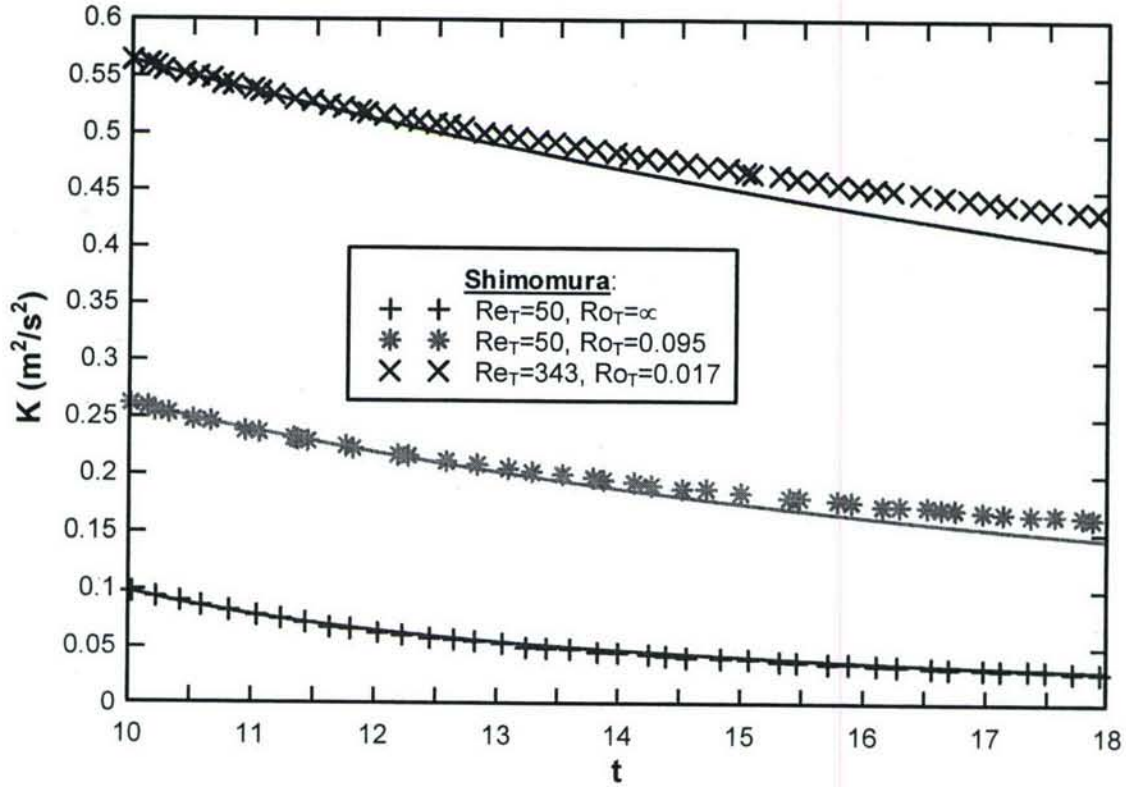

Figure 20: Rotating isotropic decay of Shimomura. Turbulent kinetic energy versus time.

In Figures 21 and 22, the asterisks represent the experimental data and the solid lines represent the predictions from our collision model.
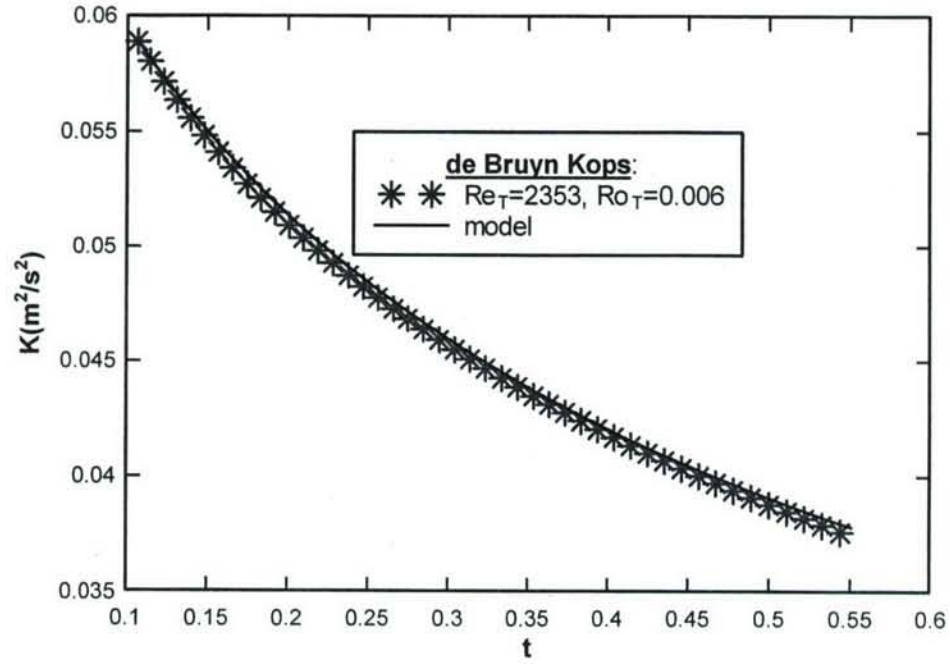
Figure 21: de Bruyn Kops rotating decaying turbulence. Turbulent kinetic energy versus time.
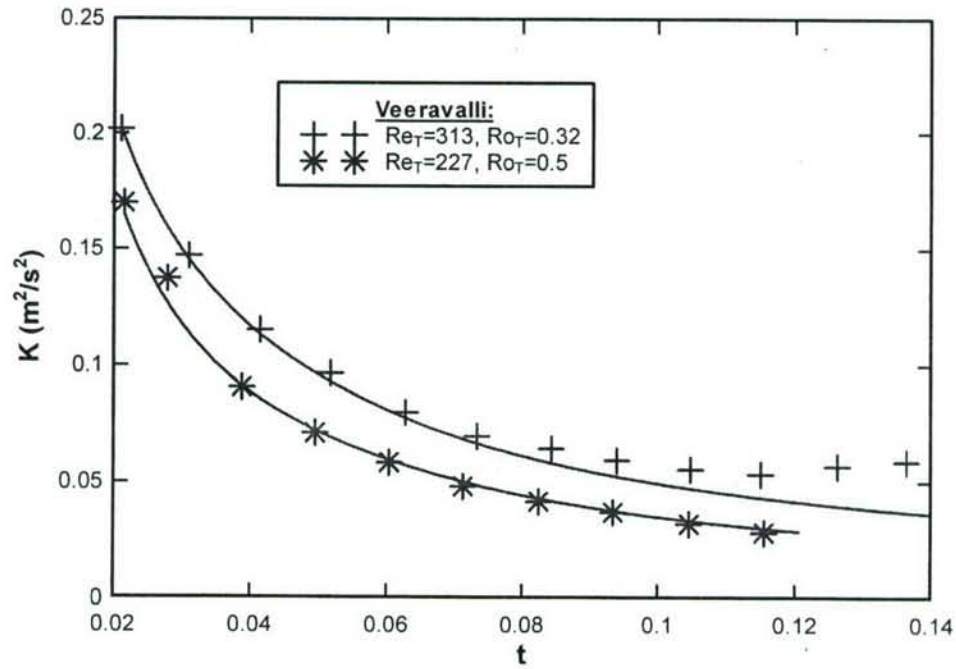

Figure 22: Veeravalli's decaying kinetic energy. Kinetic energy versus time.

In Figure 23, the asterisks represent the experimental data and the solid lines represent the predictions from the OEC model.
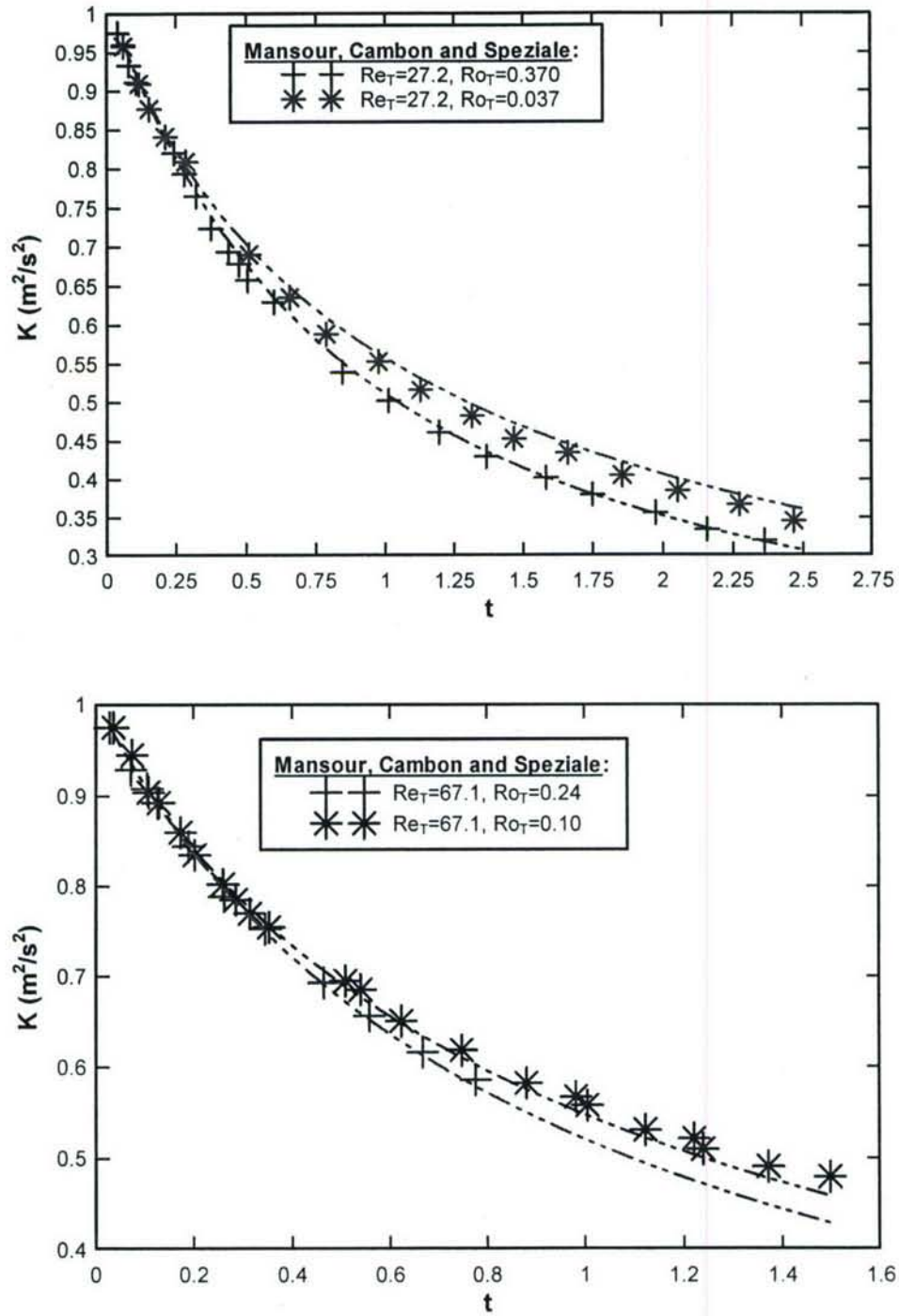

Figure 23: Rotating isotropic decay of Mansour, Cambon and Speziale. Turbulent kinetic energy versus time. a) Re_T=27.2 and b) Re_T=67.1

Rapid Distortion Theory

In turbulent shear flows, the turbulence-to-mean-shear time scale ratio defined as SK/ε varies between 0 and ∞. In the limiting cases when the ration SK/ε is exceptionally large, the evolution of the turbulence is then described exactly by rapid-distortion theory or RDT. Previous work compared this model performance to that of a standard RDT solver (*by Chartrand*). This time, we compare our model performance to that of RDT cases of Matsumoto, Blaisdell and Lee & Reynolds, with initial conditions summarized in Table7 below. Lee & Reynolds experimented three cases: axisymmetric contraction (AC), axisymmetric expansion (AE) and plane strain (PS). Matsumoto's case includes two DNS (high and low Reynolds numbers) with shear (S) deformation while Blaisdell has one elliptical (E) case.

	Lee & Reynolds			Matsumoto	Blaisdell
	(AC)	(AE)	(PS)	(S)	(E)
$\varepsilon(\text{m}^2/\text{s}^3)$	0.018	0.122	0.25	0.185	1.79
$K(\text{m}^2/\text{s}^2)$	1.0	1.0	1.0	0.2	1
$v(\text{m}^2/\text{s})$	10	10	10	1.2e-2	4.41e-2
$S\ (\text{s}^{-1})$	1	0.5	1.0	28.28	3.0
Re_T	5.59	0.82	0.4	18.18	12.75
SK/ε	55.87	4.08	4	30.6	1.68

Table 7: Initial conditions of Matsumoto and Lee& Reynolds.

Also, included in Table 8 are the non-zero mean velocity gradients for simple deformations.

	Axisymmetric contraction	Axisymmetric expansion	Plane Strain	Shear
R_{11}	S	$-2S$	S	0
R_{22}	$-\dfrac{1}{2}S$	S	$-S$	0
R_{33}	$-\dfrac{1}{2}S$	S	0	0
R_{12}	0	0	0	S
$S \equiv (2\bar{S}_{ij}\bar{S}_{ij})^{1/2}$	$\sqrt{3}S$	$2\sqrt{3}S$	$-2S$	$2S$

Table 8: Tensor matrix for simple deformations.
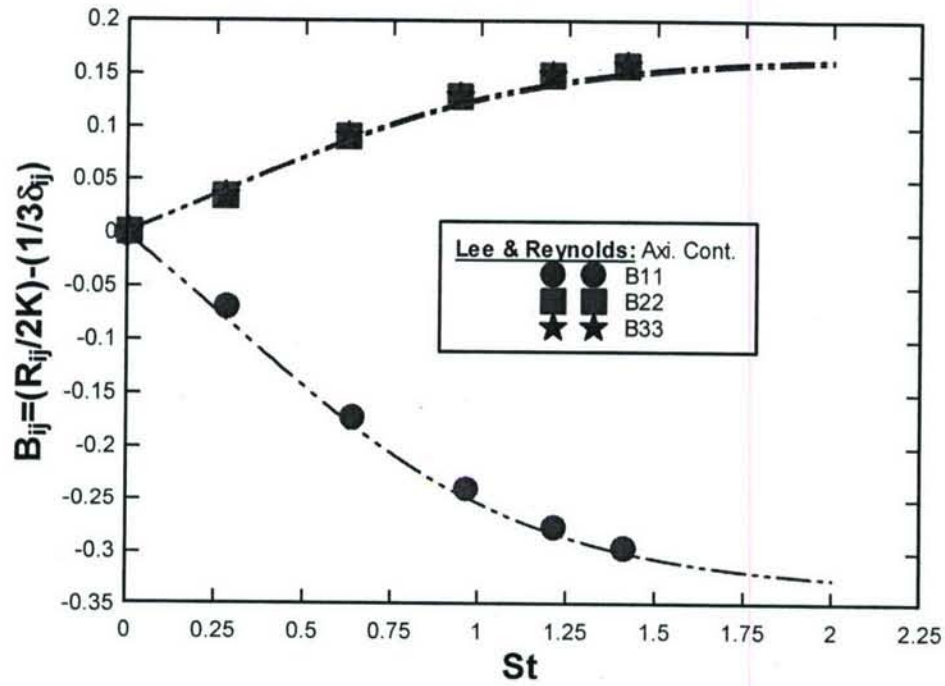
The graphs below summarize the results:

Figure 24: Lee & Reynolds' axisymmetric contraction. The dots represent the DNS and the lines represent the OEC model prediction. $SK/\varepsilon=55.9$.
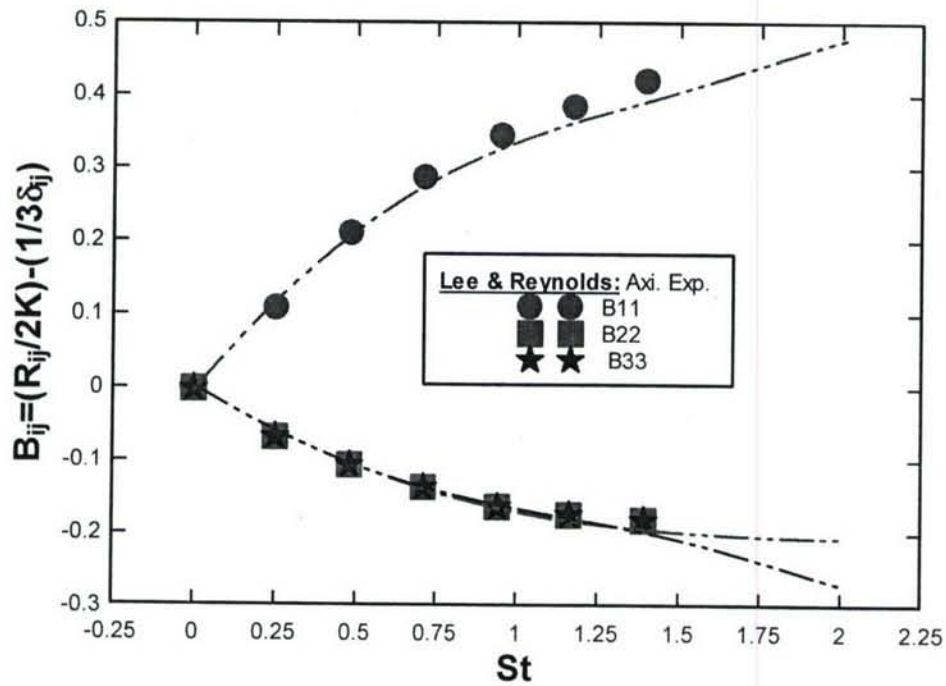

Figure 25: Lee & Reynolds' axisymmetric expansion. The dots represent the DNS and the lines represent the OEC model prediction. $SK/\varepsilon=9.08$.
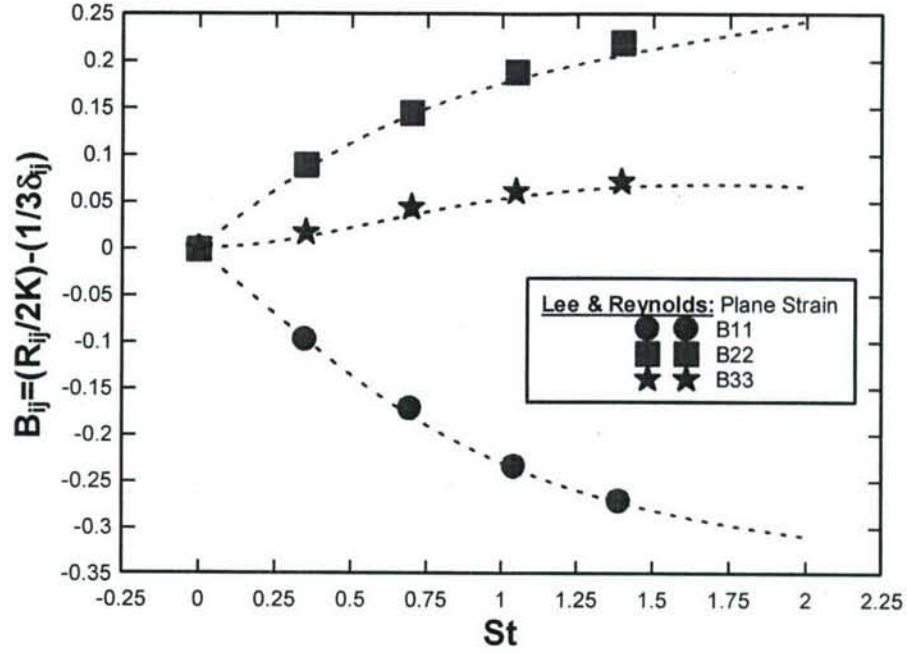
Figure 26: Lee & Reynolds' plane strain. The dots represent the DNS and the lines represent the OEC model prediction. SK/ε=4.
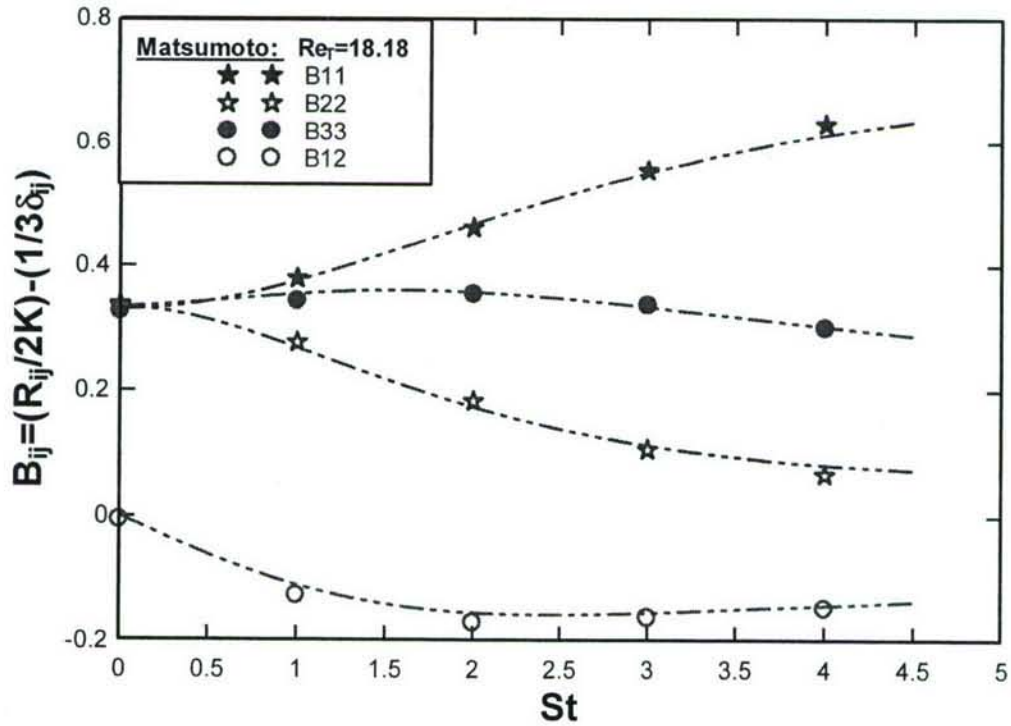

Figure 27: Matsumoto's shear deformation. The dots represent the DNS data and the lines represent the OEC model prediction. The large imposed strain (SK/ε=30.6) implies RDT is closely approximated.

The next simulation we did is based on Blaisdell's DNS. Here, the fact that both the strain ratio and the turbulent Reynolds number are small (respectively 1.68 and 12.75) in addition to the initial random field justifies the RDT approximation. Furthermore, we ran four simulations: one with only the return-model on, a second one with just the rotation model on, a third one with both return and rotation models on, and finally the RDT case (return and rotation models both turned off). Looking at the graph below, we were able to prove that both return and rotation have no effects in this case. The results are shown below in Figure 28 and 29. The dots represent the DNS and the lines show the model prediction.
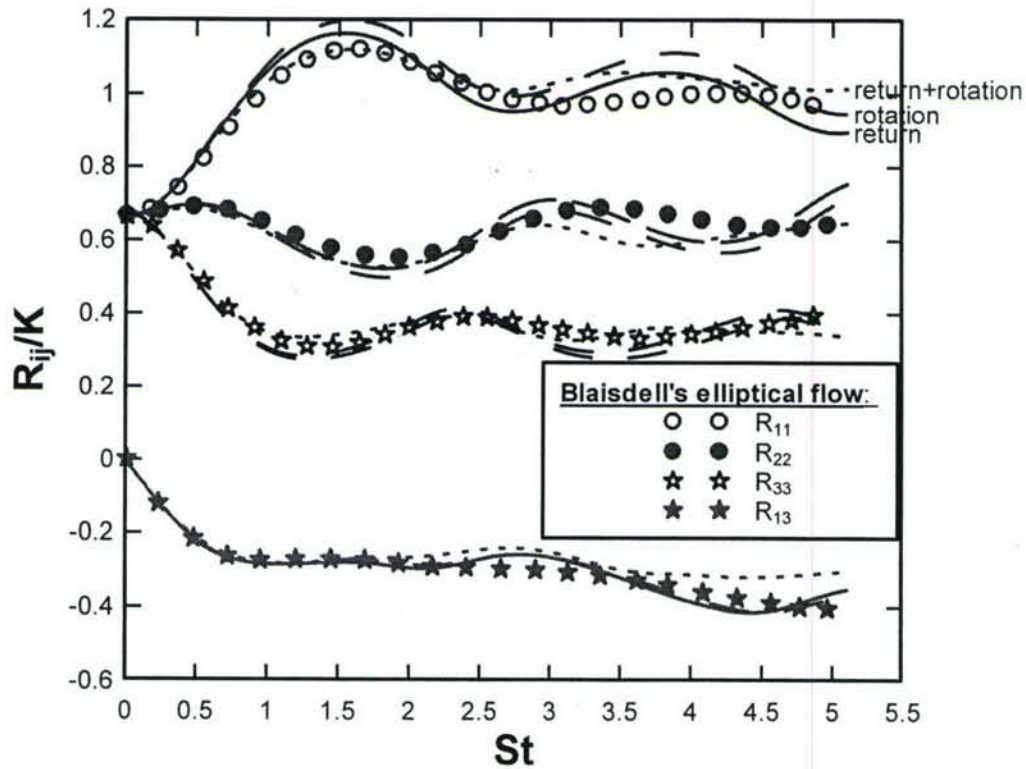

Figure 28: Blaisdell's elliptical flow with a) return model on, b) rotation model on and c) both return and rotation models on.
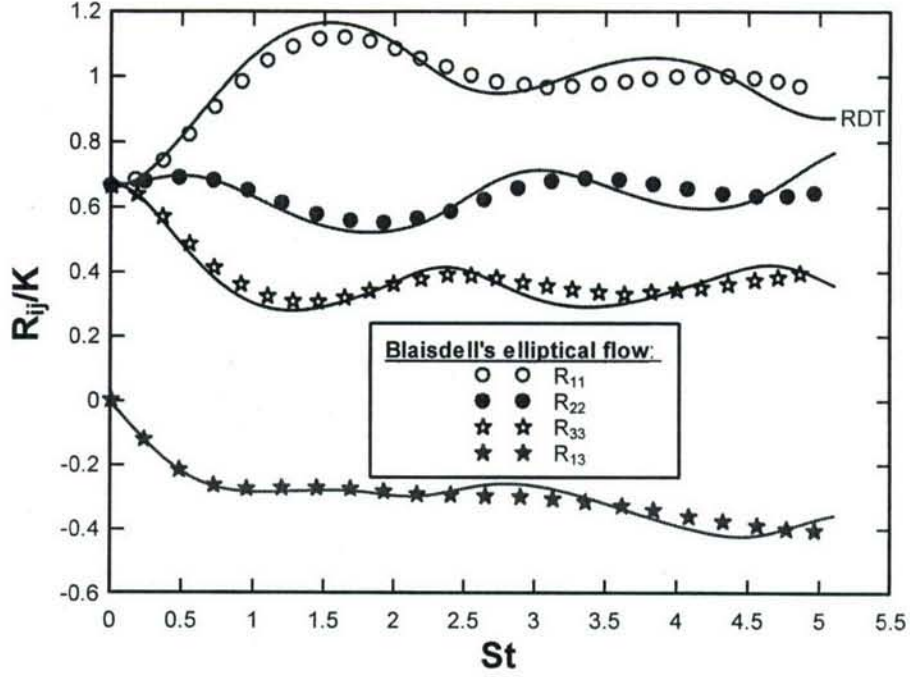
Figure 29: Blaisdell's elliptical flow: RDT

Return-to-isotropy Models

For anisotropic cases, a term to model the return to isotropy behavior of turbulent flows was introduced. From equation (7a), the term the corresponds to the return-to-isotropy model for the Reynolds stresses is,

$$\widehat{\left(\tfrac{1}{\tau_R}\right)}D_{ij} \tag{17}$$

The oriented-eddy collision model includes two types of return representations $\hat{R}_{ij}$ and k-return.

$\hat{R}_{ij}$-return model

D_{ij} was modeled in the following ways:

$$D_{ij}^{A} = C_R\left[\hat{R}_{ij} - \hat{K}\left(\delta_{ij} - \tfrac{k_i k_j}{k^2}\right)\right] \tag{18a}$$

$$D_{ij}^{B} = C_R\left[\hat{R}_{ij} - \tfrac{K}{N}\left(\delta_{ij} - \tfrac{k_i k_j}{k^2}\right)\right] \tag{18b}$$

$$D_{ij}^{C} = \left(\left(\delta_{il} - \tfrac{k_i k_l}{k^2}\right)\tfrac{R_{ls}}{K}\hat{R}_{sj}\left[\tfrac{K^2}{R_{ls}R_{sl}}\right] + \left(\delta_{jl} - \tfrac{k_j k_l}{k^2}\right)\tfrac{R_{ls}}{K}\hat{R}_{si}\left[\tfrac{K^2}{R_{ls}R_{sl}}\right] - \hat{R}_{ij}\right) \tag{18c}$$

$$D_{ij}^{D} = \left[\tfrac{K}{N}\tfrac{\hat{R}_{is}\hat{R}_{sj}}{\hat{R}_{nm}\hat{R}_{nm}} - \hat{R}_{ij}\right] \tag{18d}$$

$$D_{ij}^{E} = \left(\tfrac{K^2}{R_{ls}R_{sl}}\tfrac{(R_{is}\hat{R}_{sj} + R_{js}\hat{R}_{si})}{K} - \hat{R}_{ij}\right) \tag{18e}$$

34

The first two equations are modeled after Rotta's Reynolds Stress Transport (RST) return models. That is, both equations (18a) and (18b) work by relaxing each individual Reynolds stress towards an isotropic state (e.g. from an ellipse to a sphere) with (D_{ij}^{B}) or without (D_{ij}^{A}) regard to the other eddies. The only difference between the two equations is that one uses the individual kinetic energy of each eddy ($\hat{K}$), while the second equation uses the average global kinetic energy ($\frac{K}{N}$); thus we refer to D_{ij}^{A} as Rotta-L (Local Rotta) and D_{ij}^{B} as Rotta-G (global Rotta). C_R is a tuned constant that we determined as 4.0 in the case of Rotta-L and 2.5 for Rotta-G. Note that equations (18c), (18d) and (18e) do not have a tunable constant. Those were generated by Perot & Chartrand.

k-return Models

This k-return model is part of the orientation equation (7b) and corresponds to:

$$\widehat{\left(\frac{1}{\tau_K}\right)} m_i \tag{19}$$

The term m_i here was modeled two ways:

$$m_i^{A} = -C_{K1}\left(3\frac{k^2}{\overline{k^2}}K_{ki} - \delta_{ki}\right)k_k \tag{20a}$$

with $\overline{k^2} = \frac{1}{N}\sum k^2$ and $K_{ki} = (\frac{1}{N}\sum k_k k_i)/(\frac{1}{N}\sum k^2)$

$$m_i^{B} = -C_{K2}\left(3\frac{k^2}{\overline{k^2}}N_{ki} - \delta_{ki}\right)k_k \tag{20b}$$

with $N_{ki} = \frac{1}{N}\sum(k_k k_i / k^2)$

The first equation is referred to as the "K_{ij} return model" while the second one is the "N_{ij} return model". N_{ij} depends only on anisotropy in the orientations while K_{ij} also responds to anisotropy in the lengths of the eddies. C_{K1} and C_{K2} are tuning constants that we determined to be respectively 4.0 and 1.0. Based on numerous simulations, we determined K_{ij} to be the best performing return case as shown below in Figure 30.

At first it seems as the K_{ij}-return model performs better than the N_{ij}. However, looking closely, it is really difficult to come up with a conclusion. K_{ij} seems to work best on the R_{ii} terms while N_{ij} best performs on the non-diagonal elements. It is our goal to further investigate this as part of the future work.
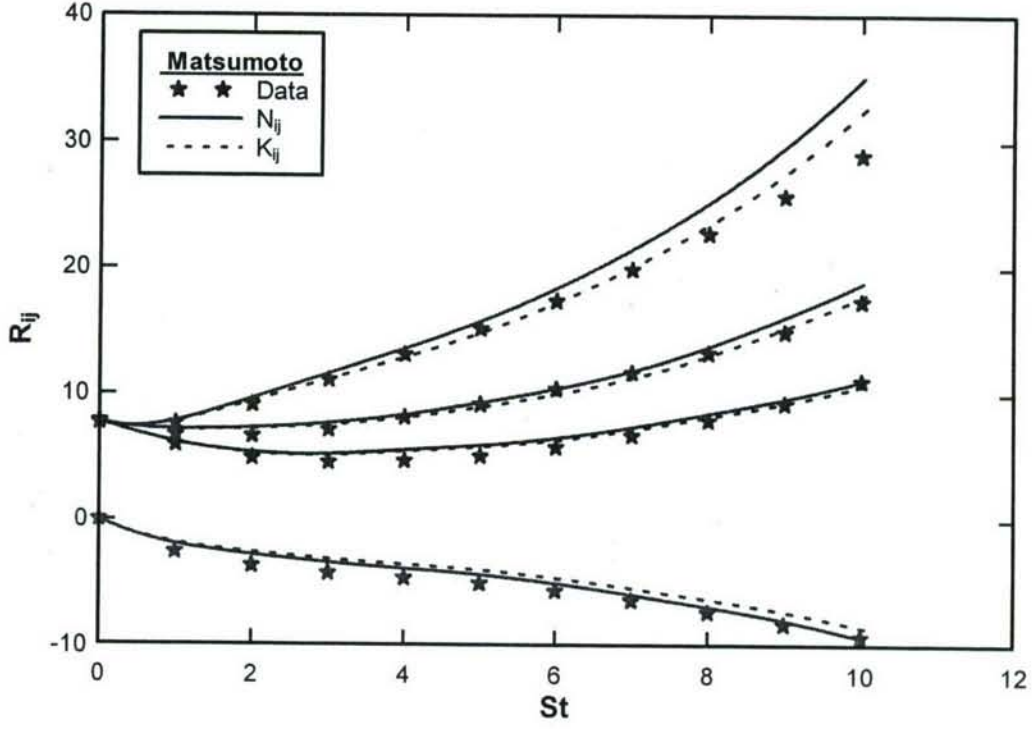
Figure 30: m_i^A and m_i^B model comparisons

As previously mentioned, (C_{K1}, C_{K2}) are tuning constants that we determined to be respectively (4,10) for N_{ij}, and (1,4) for K_{ij}.

Shear/Strain Flows

In this section, we used various DNS as well as experimental cases to test our model performance; primary in the Reynolds stresses analysis of shear flows. Tables 9 and 10 below provide a summary with the values of the constants C_R and C_K:

	Matsumoto	LePenven A	LePenven B
SK/ε	4.71	0.43	0.33
Re_T	152	612	846
(C_R, C_K)	(4,10)	(4,10)	(4,10)
Strain Tensor	$\begin{pmatrix} 0 & 30 & 0 \\ 0 & 0 & 0 \\ 0 & 0 & 0 \end{pmatrix}$	$\begin{pmatrix} 5.48 & 0 & 0 \\ 0 & 1.99 & 0 \\ 0 & 0 & -7.47 \end{pmatrix}$	$\begin{pmatrix} 8.86 & 0 & 0 \\ 0 & -2.36 & 0 \\ 0 & 0 & 6.50 \end{pmatrix}$

Table 9: Matsumoto and LePenven summary using (Rotta-L, K_{ij}), which is (D_{ij}^A, m_i^A)

36

	Hallback -PS		
Re$_T$	11		
(C_R, C_K)	(1,4)		
SK/ε	9	3	1
Strain Tensor	$\begin{pmatrix} 4.36 & 0 & 0 \\ 0 & -4.36 & 0 \\ 0 & 0 & 0 \end{pmatrix}$	$\begin{pmatrix} 1.46 & 0 & 0 \\ 0 & 0 & 0 \\ 0 & 0 & -1.46 \end{pmatrix}$	$\begin{pmatrix} 0.49 & 0 & 0 \\ 0 & 0 & 0 \\ 0 & 0 & -0.49 \end{pmatrix}$

Table 10: Hallback's summary using (Rotta-L, K$_{ij}$) for Plane Strain

Numerical Results: return-to-isotropy and shear/strain deformation

To illustrate the return-to-isotropy above, three different cases were used: LePenven, Matsumoto and Hallback. Only cases that are highly dependent on return-to-isotropy were used to determine the values of our constants as well as to validate the models. All initial conditions are shown above in Tables 9 and 10. The results are shown in Figures 31 and 32.
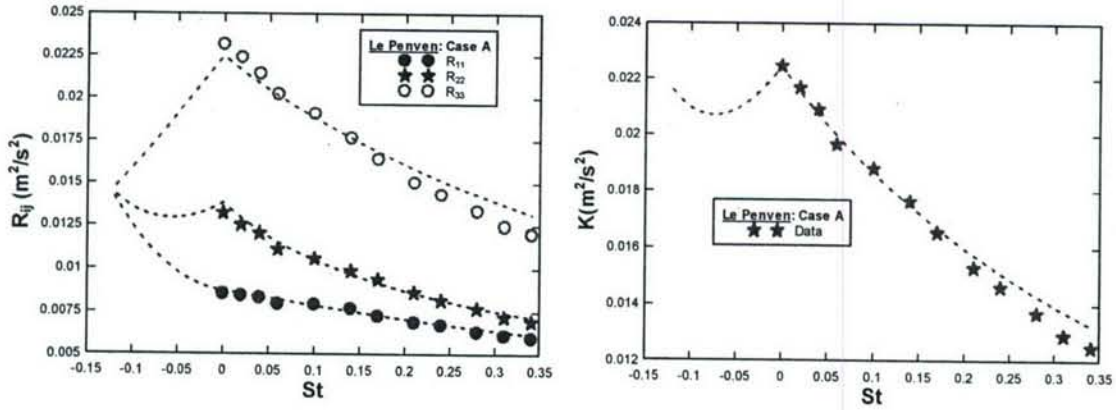

Figure 31: Le Penven - case A. a) Reynolds stresses and b) Kinetic energy
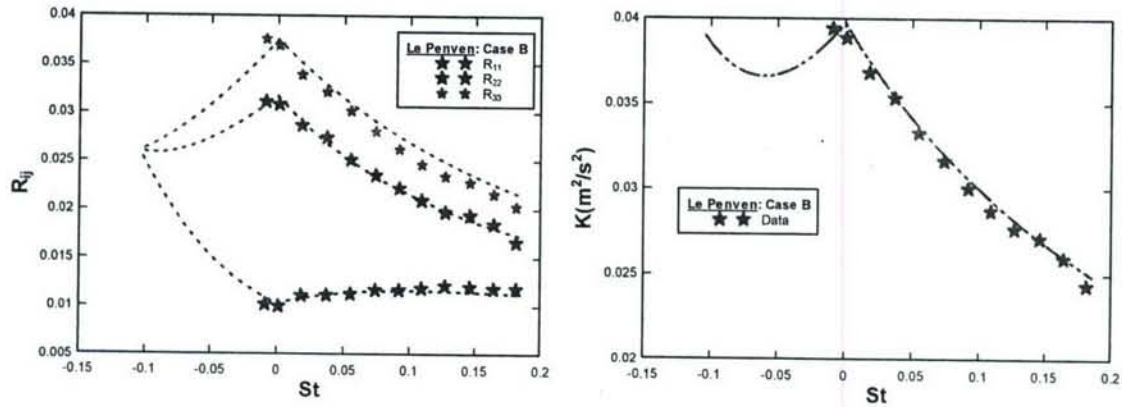

Figure 32: Le Penven - case B. a) Reynolds stresses and b) Kinetic energy

Correspondingly, the oriented-eddy collision prediction was compared to the homogeneous shear and strain flows: Matsumoto (Figure 33), and Hallback PS (Figure 34):
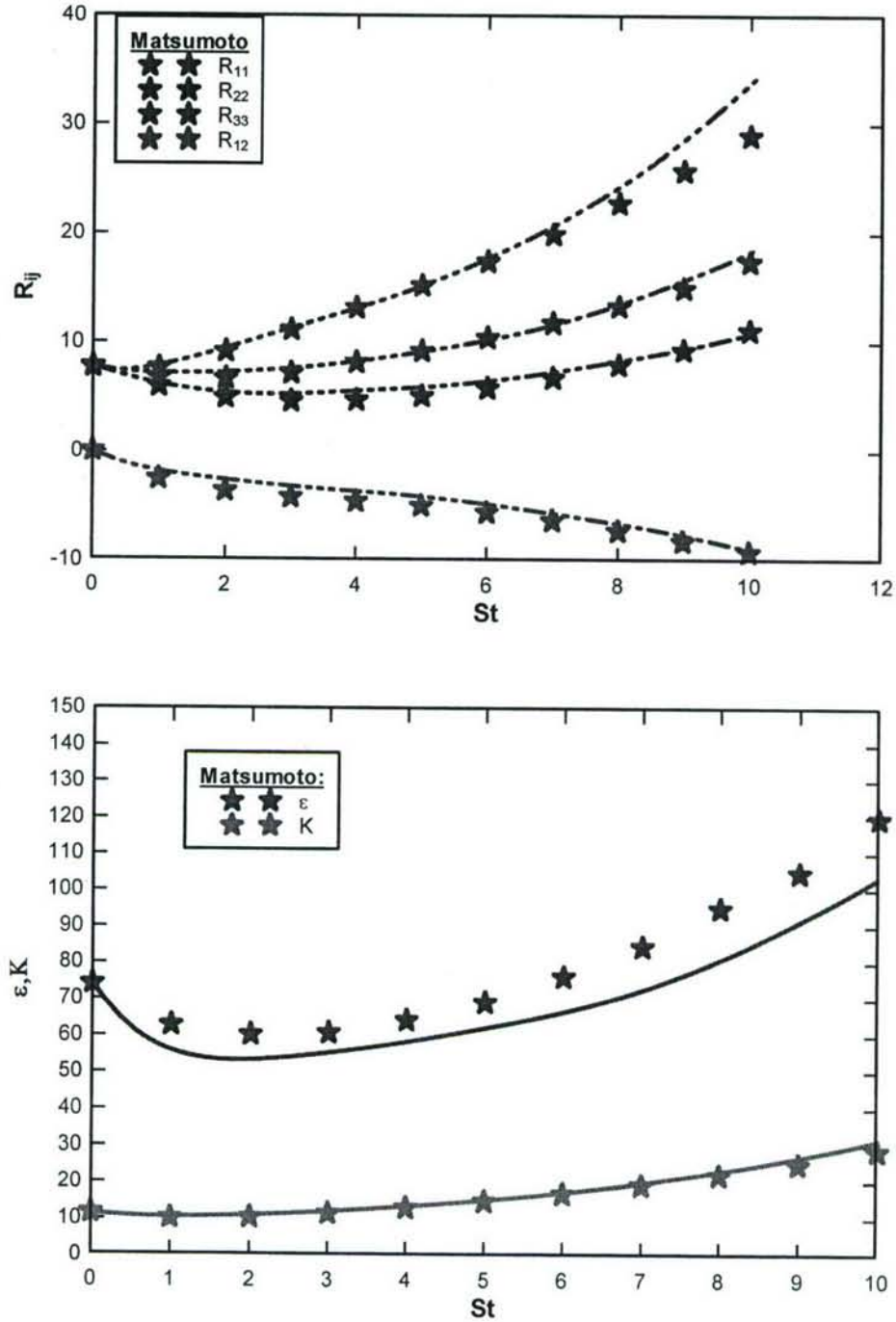

Figure 33: Matsumoto's shear deformation. The dots represent his DNS and the lines represent our model prediction. a) Reynolds stresses and b) Dissipation and kinetic energy
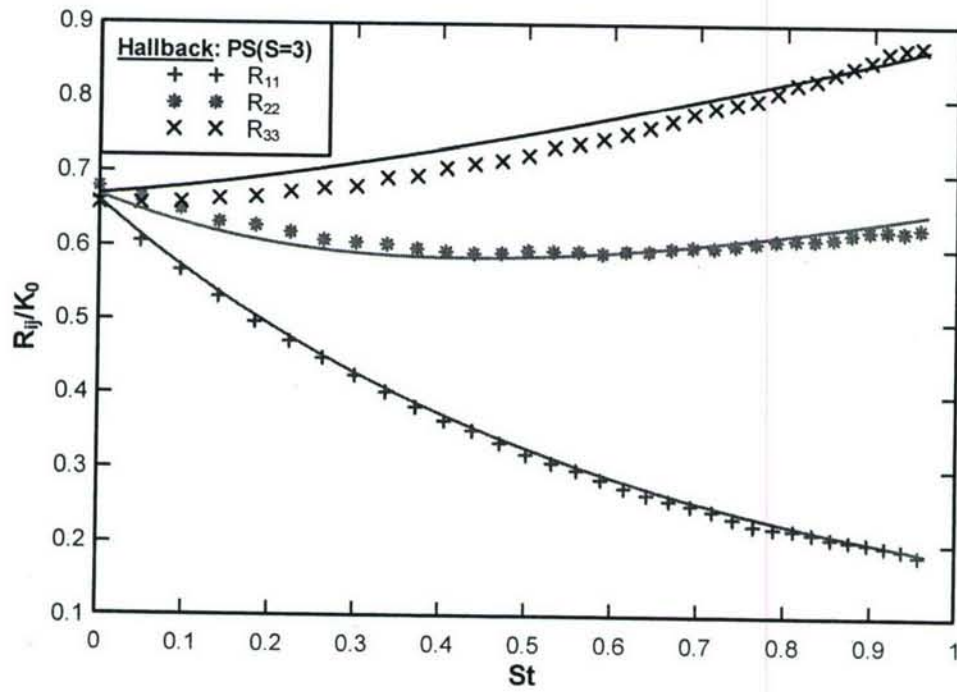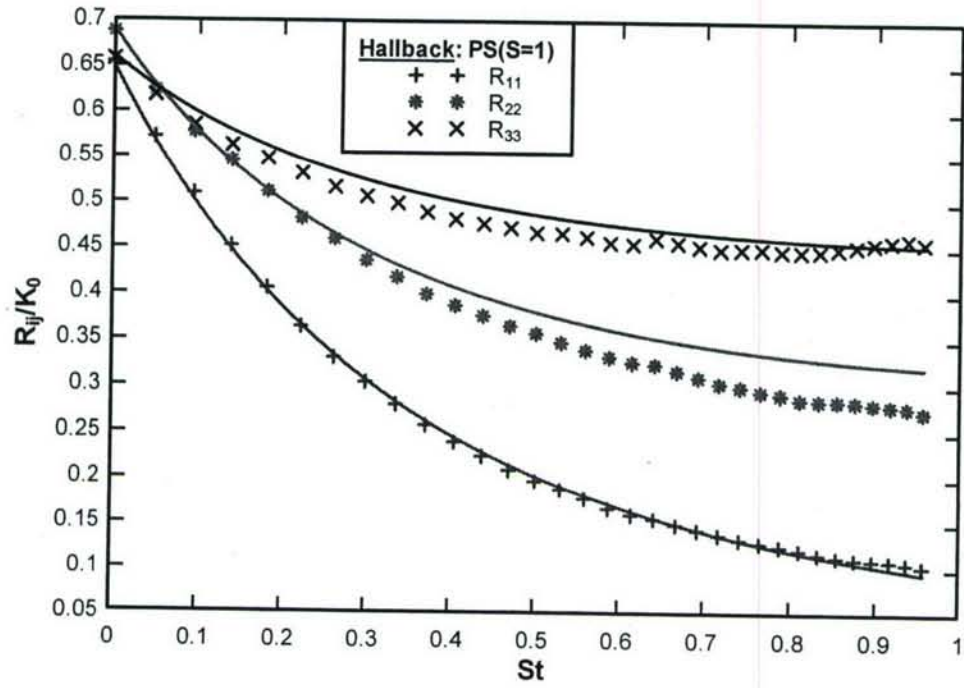
Figure 34: Hallback – Plane Strain a) S=3 and b) S=1

Diffusion

In equations (7a) and (7b) the final terms, $\nabla\left((\nu+\nu_T)\nabla\hat{R}_{ij}\right)$ models the diffusive action of the Reynolds stresses while $\nabla\left((\nu+\nu_T)\nabla k_i\right)$ accounts for the diffusive action of the orientation vectors k_i. In one-dimension, $\nabla\left((\nu+\nu_T)\nabla\hat{R}_{ij}\right)$ corresponds to

$$\frac{\partial}{\partial y}(\nu+\nu_t)\frac{\partial\hat{R}_{ij}}{\partial y} \tag{21}$$

ν is the fluid viscosity while ν_t corresponds to the eddy viscosity. We defined local and global eddy viscosities. As mentioned before, "local" implies that all calculations are done locally. In this case, the model uses a local ν_t that is defined as

$$\nu_t^L = C_L\frac{(\hat{K})^2}{\varepsilon} \tag{22a}$$

with $\hat{K}=\frac{1}{2}\hat{R}_{ii}$ and $C_L=1$. Regarding the global eddy viscosities, two equations that are referred to as *globabl1* and *global2* $\left(\nu_t^{G1}\text{ and }\nu_t^{G2}\right)$ are currently being evaluated. The *global1* and *global2* are similar, with the only difference that in the first case, the local kinetic energy and dissipation are being summed *before* dividing, whereas in the second case, the summation is done *after* the division. These concepts are illustrated below,

$$\nu_t^{G1} = C_{G1}\frac{1}{N}\left[\frac{\Sigma\left(\hat{K}^2\right)}{\Sigma(\varepsilon)}\right] \tag{22b}$$

$$\nu_t^{G2} = C_{G2}\frac{1}{N}\left[\Sigma\left(\frac{\hat{K}^2}{\varepsilon}\right)\right] \tag{22c}$$

where $C_{G1}=C_{G2}=1$ and Σ implies summation over the orientations.

As expected for isotropic flows (the orientations vectors all have then same length), both global eddy viscosity formulas $\left(\nu_t^{G1}\text{ and }\nu_t^{G2}\right)$ performed equally as shown in Figure 35 below. The comparison was done using the DNS of Carati:
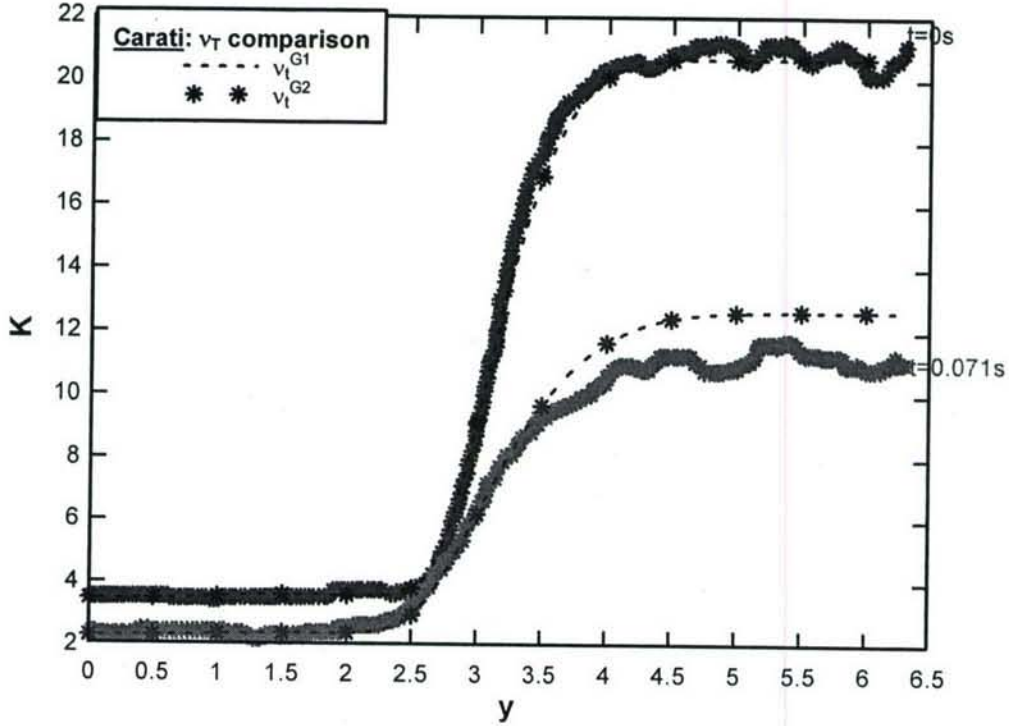
Figure 35: Eddy viscosity comparison for both global equations

After implementing the diffusion in the code along with all three variants of the eddy viscosity various simulations were conducted in order to determine the efficacy of the eddy collision model. It is important to mention that the kinetic energy decay is no longer homogeneous (as previously) but instead is also spatially dependent. In the diffusion case, at one fixed time t, we are looking at both the kinetic energy and dissipation at different locations (y). The first step in the analysis is to determine which eddy viscosity equation best models the diffusion process. Starting with v_t^{G1} (22a), various simulations were conducted as part of the evaluation process. The first simulation was run against that of Chasnov and shows the diffusion process at different times t. Chasnov's flow is inhomogeneous with the following characteristics: shearless, irrotational and isotropic with periodic boundary conditions. Note that in order to reduce the time step, we interpolated the original data as represented by the solid blue line.

Next in Figure 36, we looked at the diffusion evolution at times t=1.375, 4.125 and 9.625 seconds. The asterisks represent the data and the matching solid blue lines correspond to our simulations.
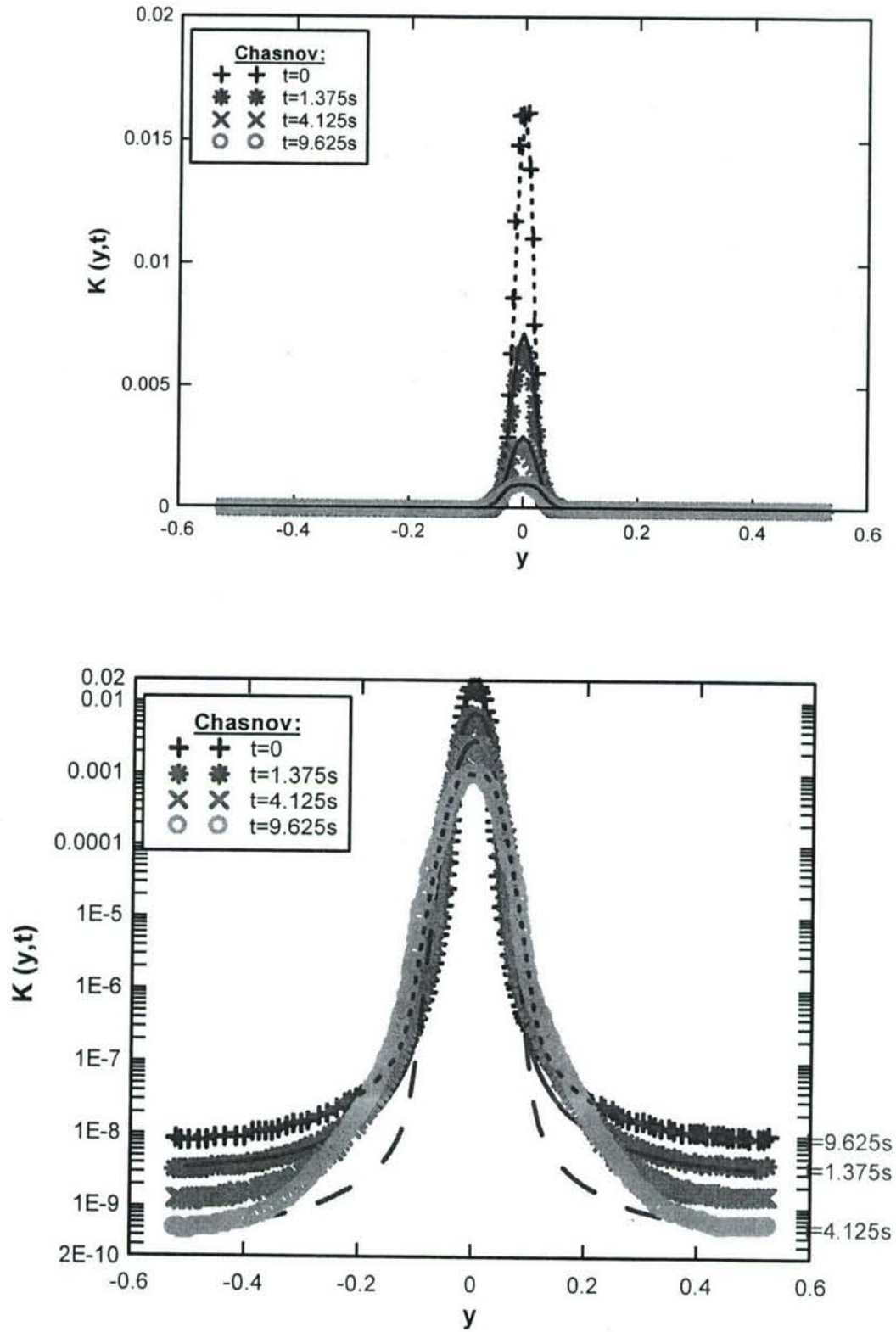
Figure 36: Kinetic Energy versus position at different times t. The matching blue lines correspond to the OEC simulations. a)linear-linear plot and b)log-linear plot.

The second diffusion simulation matched that of Gilbert. Gilbert assumes a shearless, irrotational and homogeneous flow. In addition, the flow has some levels of anisotropy. The stars represent data from Gilbert at times t=0, 0.0292, 0.0402, 0.0764, 0.0884, 0.1154, 0.1274, 0.1634 and 0.2024 seconds. The matching solid lines correspond to the simulations.
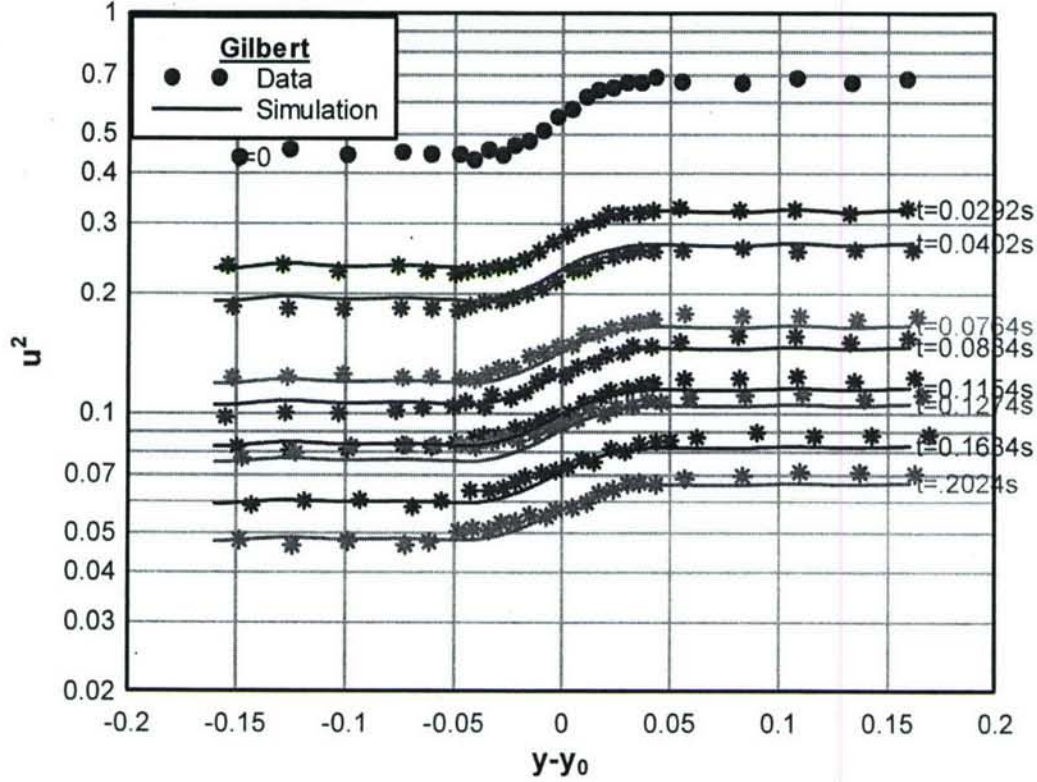

Figure 37: R_{11} (kinetic energy component) versus position. The stars represent data from Gilbert at times t=0, 0.0292, 0.0402, 0.0764, 0.0884, 0.1154, 0.1274, 0.1634 and 0.2024 seconds. The matching solid lines correspond to the OEC simulations.

The final set of data that was looked at is a more recent one (2003) and was published by Carati. Carati's data is unique in a sense that we have access to both the kinetic energy and the dissipation rate. Here although not ideal, we used zero boundary conditions compared to periodic conditions in the two cases above (Chasnov, Gilbert). For reasons that remain unclear at this time, the OEC isotropic simulations decay a little faster than expected. The results obtained are shown below in Figures 38 and 39:
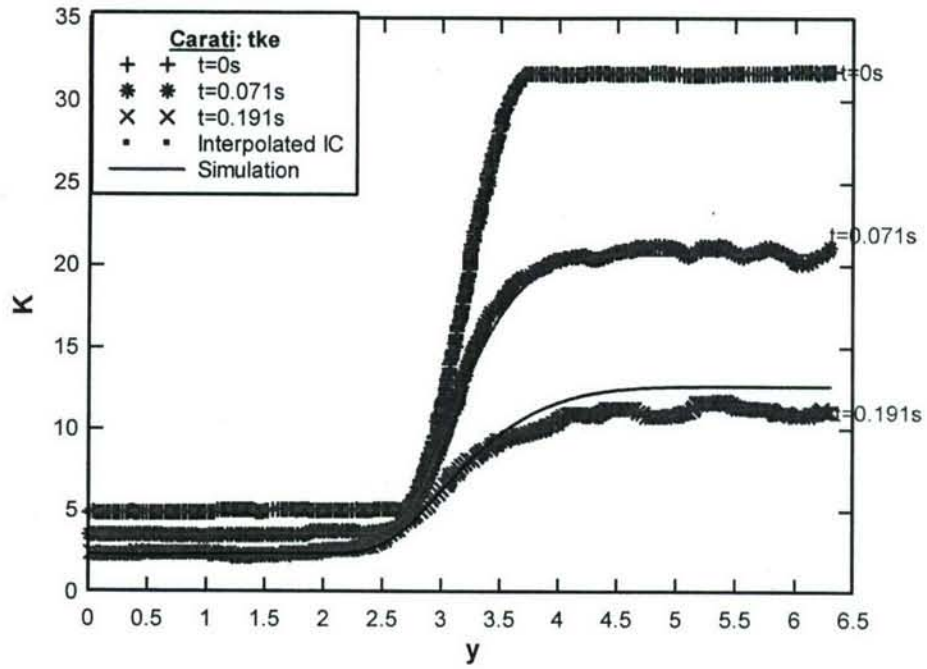
Figure 38: Kinetic Energy versus position at different times t. The stars represent data from Carati at times t=0, 0.071 and 0.191 seconds. The matching solid lines correspond to our simulations.
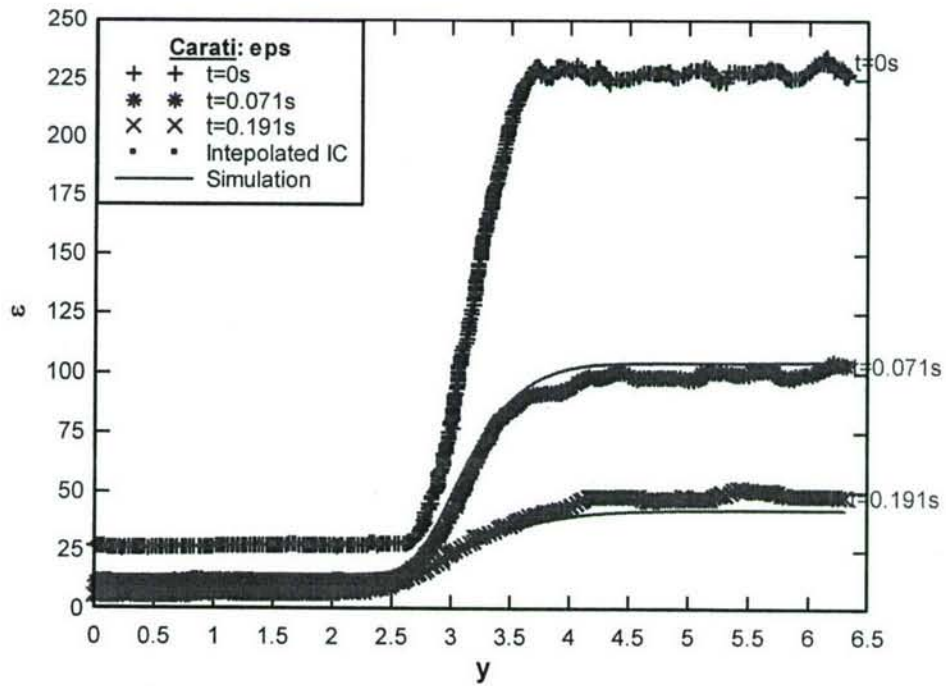

Figure 39: Dissipation versus position at different times t. The stars represent data from Carati at times t=0, 0.071 and 0.191 seconds. The matching solid lines correspond to our simulations.

44

Conclusions & Future Work

This project has allowed us to demonstrate that oriented-eddy collisional (OEC) models are an interesting, accurate, and viable approach to turbulence modeling. We have demonstrated that:

- Models exist in the regime between LES and RANS that have very attractive cost and accuracy attributes for current day design.

- It is possible to increase the physics in turbulence models and reduce the number of tuned constants, while still having a cost effective model that can run on a PC.

- The structure (orientation) of turbulence is just as import as the magnitude of the fluctuations. Models which represent structure have huge advantages in capturing the turbulence physics.

- The model can be interpreted as a model for the evolution of the two-point correlation. Critical to this model – is decomposing the two-point correlation into self-similar 'modes'.

As with any turbulence model, a great deal of work remains to validate this model. In this project we have clearly demonstrated that the approach is extensible and can accurately predict a wide variety of quite different but fundamental turbulent flow situations.

Future work will complete the modeling of wall effects. In addition, we expect this model to predict transition very well, and this will be demonstrated. Finally, this model will be implemented in a 3D, unstructured, parallel, Navier-Stokes code so that more complex and practical flow situations can be tested.

Bibliography

R. S. Rogallo and P. Moin, Numerical simulation of turbulent flows, *Annual Rev. Fluid Mech.* **16**, 99-137, 1984.

P. R. Spalart, Strategies for turbulence modeling and simulations, Engineering Turbulence Modelling and Experiments 4, Rodi and Laurence, eds. Elsevier, 1999.

O. Reynolds, On the dynamical theory of viscous incompressible fluids and the determination of the criteria, *Philos. Trans. R. Soc. London A* **186**, 123-161, 1895.

M. Germano, Turbulence: the filtering approach, *J. Fluid Mech,*. **238**, 325-336, 1992.

S.A Orzag, V. Yakhot, W.S. Flannery, F. Boysan, D. Choudhury, J. Marusewski and B. Patel, B., Renormalization group modeling and turbulence simulations", So, R.M.C., Speziale, C.G. and Launder, B.E. (eds.), Near-wall turbulent flows. Elsevier Science Publisher, 1993

P.A. Durbin, Near-wall turbulence closure modeling without 'damping functions', Theoret. Comput. Fluid Dynamics **3**, 1-13, 1991.

W. C. Reynolds, Effects of rotation on homogeneous turbulence, Proc. Of the 10th Australasian Fluid Mech. Conf. pp. 1-6, Melbourne, 1989.

C. G. Speziale, Analytical methods for the development of Reynolds stress closures, *Annual Rev. Fluid Mech.* **23**, 107-157, 1991.

M. J. Lee & W. C. Reynolds, Numerical experiments on the structure of homogeneous turbulence, Report TF-24, Thermosciences Division, Dept. of Mech. Eng., Stanford University, 1985.

A. Matsumoto, Y. Nagano and T. Tsuji, Direct Numerical Simulation of Homogeneous Turbulent Shear Flow, 5th Symposium on Computational Fluid Dynamics, pp. 361-364, 1991.

G. Compte-Bellot and S. Corrsin, Simple Eularian time correlations of full and narrow-band velocity signals in grid generated isotropic turbulence, *J. Fluid Mech.*, **48**, 273-337, 1971.

W. C. Reynolds and S. C. Kassinos, One-point modelling of rapidly deformed homogeneous turbulence, *Proceedings of the Royal Society of London A*, 451, Osborne Reynolds Centenary Volume, p. 87-104, 1995.

P. R. Van Slooten and S. B. Pope, PDF modeling for inhomogeneous turbulence with exact representation of rapid distortions, *Physics of Fluids*, 9(4):1085, 1997.

Von Karman, T. & Howarth, L. 1938, "On the statistical theory of isotropic turbulence", *Proc. Royal Soc. London Ser. A*, **164**, 192.

Saffman, P. G., 1967, "Note on decay of homogeneous turbulence," *Physics of Fluids*, **10**, 1349, (1967).

Chasnov, J. R, 1997, "Decaying turbulence in two and three dimensions", Advances in DNS/LES, Greyden Press, Columbus, Ohio.

Mansour, N. N., & Wray, A. A., 1994, "Decay of isotropic turbulence at low Reynolds number", *Phys. Fluids*, **6** (2), 808-814.

S. M. de Bruyn Kops and J. J. Riley, 1998, "Direct numerical simulation of laboratory experiments in isotropic turbulence", *Phys. Fluids*, **10**, 2125-2127.

Yu, H., Girimaji, S. S. & Luo, L.-S., 2005, "DNS and LES of decaying isotropic turbulence with and without frame rotation using a lattice Boltzmann method", J. Comput. Phys., **209**, 599-616.

J. B. Perot & C. Chartrand, "Modeling Return to Isotropy Using Kinetic Equations," Phys. of Fluids, **17** (3), (2004).

G. A. Blaisdell & K. Shariff, "Simulation and modeling of the elliptic streamline flow". *Proceedings of the 1996 Summer Program*, Center for Turbulence Research, NASA Ames/Stanford Univ., 443-446, (1996)

J. B. Perot and P. Moin, "A Near Wall Model for the Dissipation Tensor," Eleventh Australasian Fluid Mechanics Conference, Hobart, Tasmania, Australia, 13-18 (1992).

L. Le Penven, J. N. Gence, and G. Comte-Bellot, "On the Approach to Isotropy of Homogeneous Turbulence: Effect of the Partition of Kinetic Energy Among the Velocity Components", Frontiers in Fluid Mechanics, 1-21 (1985).

J. B. Perot & S. Natu, A model for the dissipation tensor in inhomogeneous and anisotropic turbulence, Submitted to *Phys. Fluids*, May 2003.

S. G. Saddoughi and S. V. Veeravalli, "Local isotropy in turbulent boundary layers at high Reynolds number," J. Fluid Mech. **268**, 333 -372 (1994).

M. J. Lee and W. C. Reynolds, "Numerical experiments on the structure of homogeneous turbulence," Standford University Tech. Rep TF-24 (1985).

J. B. Perot and P. Moin, "Shear-Free Turbulent Boundary Layers, Part I: Physical Insights into Near Wall Turbulence," J. Fluid Mech. **295**, 199-227 (1995).

J. B. Perot & P. Moin, "Shear-Free Turbulent Boundary Layers, Part 2: New concepts for Reynolds stress transport equation modelling of inhomogeneous flows," J. Fluid Mech. **295**, 229-245 (1995).

S. Tavoularis and S. Corrsin, "Experiments in nearly homogeneous turbulent shear flow with a uniform mean temperature gradient. Part1," J. Fluid Mech. **104**, 311-347 (1981).

S. M. de Bruyn Kops & J. J. Riley, Direct numerical simulation of laboratory experiments in isotropic turbulence, *Phys. Fluids*, **10** (9), 2125-2127, 1998.

M. Hallbäck, J. Groth & A. V. Johansson, "A Reynolds stress closures for the dissipation in anisotropic turbulent flows," 7th Symposium on Turbulent Shear Flows, Stanford University, August. (1989).

M. Hallbäck, J. Groth & A. V. Johansson, "An algebraic model for nonisotropic turbulent dissipation rate in Reynolds stress closures," Phys. Fluids, **2** (10, 1859-1866, (1990).

K. S. Choi and J. L. Lumley, "Turbulence and Chaotic Phenomena in Fluids," *Proceedings of the IUTAM Symposium* (Kyoto, Japan), edited by T. Tatsumi, North-Holland, Amsterdam, p. 267, (1984)

M. Yamamoto and C. Arakawa, "Study on the Pressure-Strain Term in Reynolds Stress models." *Proceedings of the Eighth Symposium on Turbulent Shear Flows*, Technical University of Munich, Munich, Germany, pp. III-17-1 – III-17-2 (1991).

University of Massachusetts, A105250
Mechanical & Industrial Engineering Dept.
Engineering Laboratory, Room 219
160 Governors Drive
AMherst, MA 01003-9265